

Chapter 2

Convective Instability of a Boundary Layer with Temperature- and Strain-Rate-Dependent Viscosity in Terms of ‘Available Buoyancy’

Published in *Geophysical Journal International* by C. P. Conrad and P. Molnar, 139, 51-68, 1999. Copyright by the Royal Astronomical Society.

Abstract. Cold mantle lithosphere is gravitationally unstable with respect to the hotter buoyant asthenosphere beneath it, leading to the possibility that the lower part of the mantle lithosphere could sink into the mantle in convective downwelling. Such instabilities are driven by the negative thermal buoyancy of the cold lithosphere and retarded largely by viscous stress in the lithosphere. Because of the temperature dependence of viscosity, the coldest, and therefore densest, parts of the lithosphere are unavailable for driving the instability because of their strength. By comparing theory and the results of a finite element representation of a cooling lithosphere, we show that for a Newtonian fluid, the rate of exponential growth of an instability should be approximately proportional to the integral over the depth of the lithosphere of the

ratio of thermal buoyancy to viscosity, both of which are functions of temperature, and thus depth. We term this quantity “available buoyancy” because it quantifies the buoyancy of material sufficiently weak to flow, and therefore available for driving convective downwelling. For non-Newtonian viscosity with power law exponent n and temperature-dependent pre-exponential factor B , the instabilities grow super-exponentially, as described by *Houseman and Molnar* [1997], and the appropriate time scale is given by the integral of the n^{th} power of the ratio of the thermal buoyancy to B . The scaling by the “available buoyancy” thus offers a method of determining the time scale for the growth of perturbations to an arbitrary temperature profile, and a given dependence of viscosity on both temperature and strain rate. This time scale can be compared to the one relevant for the smoothing of temperature perturbations by the diffusion of heat, allowing us to define a parameter, similar to a Rayleigh number, that describes a given temperature profile’s tendency toward convective instability. Like the Rayleigh number, this parameter depends on the cube of the thickness of a potentially unstable layer; therefore, mechanical thickening of a layer should substantially increase its degree of convective instability, and could cause stable lithosphere to become convectively unstable on short time scales. We estimate that convective erosion will, in 10 million years, reduce a layer thickened by a factor of two to a thickness only 20 to 50% greater than its pre-thickened value. Thickening followed by convective instability may lead to a net *thinning* of a layer if thickening also enhances the amplitude of perturbations to the layer’s lateral temperature structure. For the mantle lithosphere, the resulting influx of hot asthenosphere could result in rapid surface uplift and volcanism.

2.1 Introduction

The Earth’s lithosphere is both denser and stronger than the underlying asthenosphere, and thus provides the negative buoyancy needed to drive convection in the mantle while at the same time significantly resisting these convective motions [e.g, *Solomatov, 1995*]. As a result, the lithosphere influences the patterns and scales of

convection that occur in the mantle. For example, *Jaupart and Parsons* [1985] find that the length scale of convection depends critically on the viscosity contrast between the boundary layer and the underlying fluid. For intermediate viscosity contrasts, the strength of the upper boundary layer causes convection to occur at wavelengths larger than those expected for an isoviscous fluid, which could explain the existence of long-wavelength plates on the Earth [e.g. *Davies*, 1988]. If the viscosity contrast is large, deformation of the boundary layer becomes sufficiently difficult that it can not participate in convection. In this case, short-wavelength instabilities, of the type described by *Howard* [1964] and observed in the laboratory by *Davaille and Jaupart* [1993], develop beneath a “rigid lid.” These convective downwellings could manifest themselves in the Earth as the downwelling of the lower, weaker, part of the mantle lithosphere into the underlying asthenosphere.

Convective removal of cold mantle lithosphere and its replacement by hot asthenosphere could manifest itself at the surface as rapid surface uplift followed by eventual extension [e.g., *Bird*, 1979; *England and Houseman*, 1989; *Houseman and Molnar*, 1997; *Molnar, England, and Martinod*, 1993; *Neil and Houseman*, 1999]. This sequence of events has been inferred for several mountain belts [*Houseman and Molnar*, 1997]. For example, the Tibetan plateau is thought to have undergone rapid uplift about 8 million years ago in response to convective removal of mantle lithosphere, triggered by mechanical thickening [e.g., *Harrison et al.*, 1992; *Molnar, England, and Martinod*, 1993].

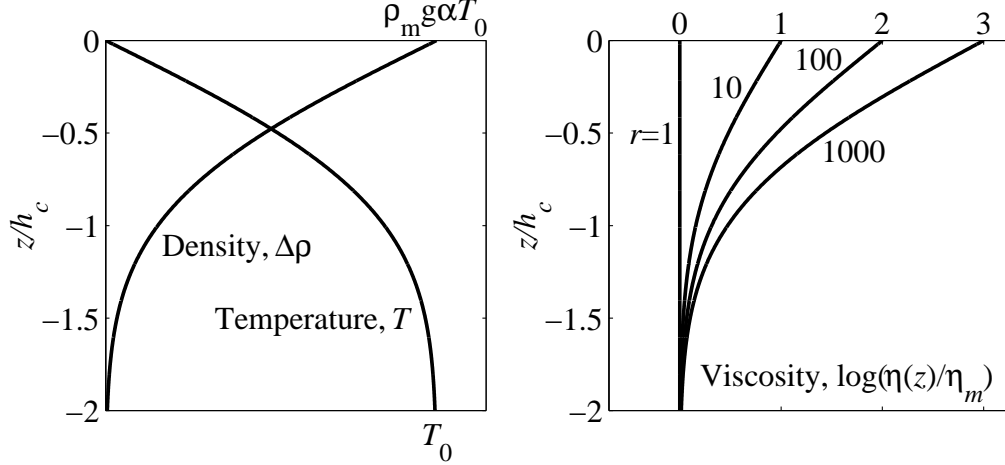
Thickening of the mantle lithosphere by horizontal shortening can enhance the gravitational instability in several ways. First, thickening forces cold lithosphere downward into the hot asthenosphere, increasing the mass excess of the thickened region. [e.g., *Fleitout and Froidevaux*, 1982; *Houseman, McKenzie and Molnar*, 1981]. Second, horizontal shortening could generate large amplitude perturbations to the background temperature structure of the lithosphere through nonuniform thickening or folding of the lithosphere [e.g., *Bassi and Bonnin*, 1988; *Fletcher and Hallet*, 1983; *Ricard and Froidevaux*, 1986; *Zuber, Parmentier, and Fletcher*, 1986]. Finally, if the lithosphere weakens with increasing strain rate, as is expected for mantle rocks

with non-Newtonian viscosity, horizontal shortening can decrease the strength of the lithosphere and thus enhance its potential for convective instability [*Molnar, Houseman, and Conrad, 1998*]. Thus, horizontal shortening could play an important role in generating convective instabilities in the lithosphere.

The degree to which the mantle lithosphere can become convectively unstable depends primarily on its density and viscosity structure. Because of the temperature dependence of mantle viscosity, the coldest, and therefore densest, part of the mantle lithosphere is also the most viscous (Figure 2.1). As a result, the gravitationally most unstable material in the lithosphere may be unavailable for driving a convective instability because of its strength. The bottom part of the mantle lithosphere is warmer, and therefore weaker, than the material that overlies it, but its warmth also makes it less dense, and therefore less prone to instability. Thus, low temperature makes lithospheric rock both dense and strong, with the former driving and the latter retarding an instability. As a result, the generation of a convective instability is determined by the lithosphere's temperature structure and the details of how viscosity and density depend on temperature. Because neither the temperature profile of the lithosphere nor its affect on viscosity are well known, it is difficult to predict whether convective instabilities can, in fact, grow in the lithosphere.

If diffusion of heat is ignored, the convective instability can be approximated as a Rayleigh-Taylor instability in which a dense layer overlies a less dense layer in a gravitational field [e.g, *Chandrasekhar, 1961*]. Gravity acting on perturbations to this unstable stratified density structure will cause these perturbations to grow, but against resisting forces due to the viscous strength of the layers. As the perturbation grows, the buoyancy forces increase, causing the instability to grow at a faster rate. For Newtonian viscosity, the amplitude of the instability initially grows exponentially with time [e.g, *Chandrasekhar, 1961*]. For non-Newtonian, strain-rate-dependent, viscosity, the instability grows super-exponentially because the effective viscosity of the fluid decreases as amplitudes, and thus strain rates, increase [*Canright and Morris, 1993; Houseman and Molnar, 1997*]. A few studies [e.g. *Conrad and Molnar, 1997; Molnar, Houseman and Conrad, 1998*] have shown that exponential or super-

Error Function Temperature Profile



Linear Temperature Profile

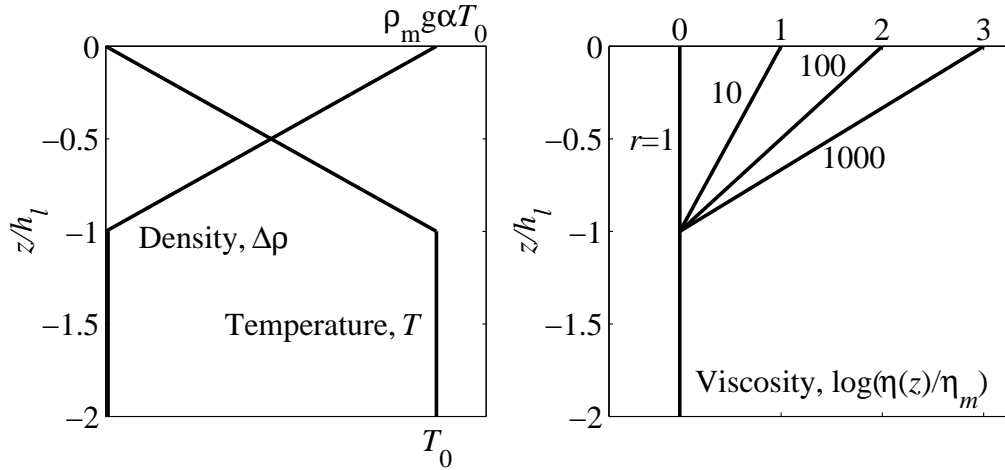


Figure 2.1: A cartoon showing the approximate variation of density (left) and viscosity (right) with depth in a boundary layer, analogous to the lithosphere. Both are the result of the variation of temperature with depth, and are given for an error-function temperature profile (top) and a linear temperature profile (bottom), which are the two initial temperature profiles studied in the numerical calculations performed here. Viscosity, which varies with temperature according to (2.43), where $\eta = B/2$, is shown relative to that of the deep fluid (asthenosphere). Plots for different $\eta(z)$ are shown by r , which is the ratio of surface viscosity to mantle viscosity. Thus, $r = 1$ represents the isoviscous case.

exponential growth rates depend critically on how viscosity varies across a layer. By combining the analysis of these previous studies with a heuristic analysis of the growth of an instability, we develop a general scaling law that enables us to estimate the growth rate of an instability from its initial temperature and viscosity structures.

The Rayleigh-Taylor analysis ignores the effects of the diffusion of heat. In a full convective instability, density perturbations are created by horizontal temperature gradients. If viscous forces are sufficiently strong, the rate at which perturbations to the temperature structure grow could be slowed to the point at which they are eliminated by thermal diffusion. If this occurs, growth of the instability stops, and the thermal structure is convectively stable. Lateral diffusion of heat diminishes short wavelength instabilities faster than longer ones, so its effects should decrease with increasing wavelength. By comparing growth rates obtained by analogy to the Rayleigh-Taylor instability to the rates at which temperature perturbations decay, we show that we can determine whether a given temperature profile will be convectively unstable for a given wavelength and temperature dependence of viscosity. We verify this using numerical solutions to the basic equations for convection, for both Newtonian and non-Newtonian rheology, and allowing for finite amplitude instabilities. Although we do not directly include horizontal shortening in our calculations, we will show that mechanical thickening of the lithosphere can cause it to become more convectively unstable, by increasing the amount of negatively buoyant material that can contribute to an instability and by diminishing the retarding effects of thermal diffusion. Thus, we present another mechanism by which convective instability is enhanced by horizontal shortening, supporting the prediction that convective instabilities are most likely to occur where the mantle lithosphere has been significantly thickened.

2.2 Theory

We begin our analysis of the convective instability of the lithosphere by exploiting a simple analysis of the Rayleigh-Taylor instability, building upon the linear analysis

presented by *Chandrasekhar* [1961], and considered further by *Conrad and Molnar* [1997] and *Houseman and Molnar* [1997]. This analysis recognizes that lithospheric temperatures increase much more rapidly with depth than the adiabatic profile and thus generate a density structure that can become unstable if perturbations to it are allowed to grow.

The deformation of a fluid is described by a strain rate, $\dot{\epsilon}_{ij}$, which is defined in terms of the components of velocity, u_i :

$$\dot{\epsilon}_{ij} = \frac{1}{2} \left(\frac{\partial u_i}{\partial x_j} + \frac{\partial u_j}{\partial x_i} \right) \quad (2.1)$$

The flow field is incompressible:

$$\dot{\epsilon}_{ii} = \frac{\partial u_i}{\partial x_i} = 0 \quad (2.2)$$

In a viscous fluid, flow occurs to balance viscous stresses and gravitational body forces:

$$\frac{\partial \sigma_{ij}}{\partial x_j} - \rho g \delta_{iz} = 0 \quad (2.3)$$

where g is the gravitational acceleration, ρ is density, δ_{ij} is the Kronecker delta, and we ignore inertial terms. The stress component, σ_{ij} , can be separated into pressure, p , and deviatoric stress, τ_{ij} :

$$\sigma_{ij} = -p\delta_{ij} + \tau_{ij} \quad (2.4)$$

We assume a nonlinear relationship between deviatoric stress, τ_{ij} , and strain rate, $\dot{\epsilon}_{ij}$, of:

$$\tau_{ij} = B \dot{E}^{(1/n-1)} \dot{\epsilon}_{ij} \quad (2.5)$$

where B is a rheological parameter, n is a power law exponent, and $\dot{E}^2 = (1/2) \sum_{i,j} \dot{\epsilon}_{ij} \cdot \dot{\epsilon}_{ij}$ is the second invariant of the strain-rate tensor. Mantle rocks are thought to deform by dislocation flow of olivine in the lithosphere, which can be described using (2.5) where n is about 3 to 3.5 [e.g., *Kohlstedt, Evans, and Mackwell, 1995*]. It is useful to

relate stress directly to strain rate as:

$$\tau_{ij} = 2\eta\dot{\epsilon}_{ij} \quad (2.6)$$

where effective viscosity, η , depends on strain rate according to:

$$\eta = \frac{B}{2}\dot{E}^{(\frac{1}{n}-1)} \quad (2.7)$$

If $n = 1$ for Newtonian viscosity, the material exhibits a linear relationship between stress and strain rate, and $\eta = B/2$ is a constant.

2.2.1 Review of Previous Studies

If viscosity is Newtonian ($n = 1$), perturbations to an unstable density structure grow exponentially with time [e.g., *Chandrasekhar*, 1961; *Conrad and Molnar*, 1997]. Thus, if Z is the magnitude of a sinusoidal perturbation in vertical displacement, and $w = \partial Z/\partial t$ is the downward velocity, both grow with the exponential growth rate q , as given by:

$$\frac{dw}{dt} = qw \quad \text{and} \quad \frac{dZ}{dt} = qZ \quad (2.8)$$

where q can be expressed as a function of the material properties of the fluid:

$$q = \frac{\Delta\rho gh}{2\eta}q'' \quad (2.9)$$

Here $\Delta\rho$ is the density difference across the unstable portion of the layer, h is a typical length scale associated the thickness of this layer, and η is the Newtonian viscosity at the bottom of the layer. The dimensionless growth rate, q'' , is a function of the variation of both density and viscosity with depth, and of the wavelength of the perturbation.

A density instability in a fluid with non-Newtonian viscosity ($n > 1$) grows super-exponentially, as described by *Canright and Morris* [1993] and *Houseman and Molnar* [1997]. As the amplitude of a growing instability increases, strain rates also increase,

so the effective viscosity η , as given by (2.7), decreases. *Houseman and Molnar* [1997] suggest approximating $\dot{E}_{zz} \sim w/h$ in (2.7) to define a time-varying effective viscosity to be used to define η in (2.9). Then, with such a definition for q in (2.9) inserted into (2.8), they obtain an expression for super-exponential growth:

$$w = \left[C'' \left(\frac{n-1}{n} \right) \frac{\Delta\rho g}{B} (h)^{(1/n)} (t_b - t) \right]^{\left(\frac{n}{1-n} \right)} \quad (2.10)$$

where t_b is the time at which velocity becomes infinite, at which point the instability must be detached from the dense layer, and C'' is a dimensionless measure of the rate of growth, equivalent to q'' and dependent on the variation of density and B with depth, and on the wavelength of the perturbation. *Houseman and Molnar* [1997] suggest the following nondimensionalization of time and length:

$$t'' = t \left(\frac{\Delta\rho gh}{B} \right)^n \quad \text{and} \quad z'' = \frac{z}{h} \quad (2.11)$$

which reduces (2.10) to:

$$w'' = \left[C'' \left(\frac{n-1}{n} \right) (t_b'' - t'') \right]^{\left(\frac{n}{1-n} \right)} \quad (2.12)$$

If $n = 1$ for Newtonian viscosity, using (2.11) to make (2.8) dimensionless yields $dw''/dt'' = q''w''$. Because the dimensionless time scale of (2.11) contains no information about the variation of density or viscosity with depth, this information must be incorporated into q'' or C'' .

2.2.2 Available Buoyancy

Because both q'' and C'' depend on the details of how density and viscosity vary with depth, their values must be redefined and recalculated for every given density and viscosity profile. In what follows, we use a heuristic analysis of a Rayleigh-Taylor instability to develop a more general scaling law to account for the variation of density and viscosity with depth in a layer. In doing so, we define new dimensionless growth

rates, q' and C' , which are distinguished from q'' and C'' by depending *only* on the wavelength of the perturbation.

Consider a layer positioned between $z = -h$ and $z = 0$ of density ρ_1 overlying a halfspace of density $\rho_2 < \rho_1$. A sinusoidal perturbation of the boundary between them creates a deviatoric stress field. Continuity of normal stress across the perturbed boundary can be expressed as a difference in stresses across a line representing the unperturbed boundary, by taking the additional overburden pressure due to the deformation into account [e.g., *Ricard and Froidevaux, 1986*]:

$$\sigma_{1,zz} - \sigma_{2,zz} = (\rho_1 - \rho_2)gZ \cos(kx) \quad (2.13)$$

where $k = 2\pi/\lambda$ is the wavenumber of the perturbation in vertical displacement and Z is its amplitude. Thus, the stresses that drive the instability are generated by the anomalous mass of material that has crossed the original boundary between the layers. These driving stresses can be separated into deviatoric stress and pressure, as shown by (2.4). The deviatoric stress, τ_{zz} , can be directly related to fluid deformation using (2.6). The fluid flow itself also creates a dynamic pressure, p , which varies laterally. The amplitudes of both τ_{zz} and p should both depend linearly on the right hand side of (2.13) because both components are associated with the perturbation to the density field, but their relative values should vary with wavenumber and depth. In the numerical studies we perform later, we find that the depth dependences of τ_{zz} and p are similar throughout a deforming layer, except where the deviatoric stress is necessarily zero, such as near a rigid boundary. As a result, we can relate the deviatoric stress directly to the total stress, and treat σ_{zz} as proportional to τ_{zz} in the following analysis, remembering that this approximation overestimates the deviatoric stress near rigid boundaries. Because the fraction of the total stress that is deviatoric depends on the wavenumber k , we proceed using only proportionalities when dealing with stress. The uncertainty in proportionality will later be accommodated in a factor that depends only on wavenumber.

To develop a simple scaling law that takes into account the variation of material

properties with depth, we must apply the driving stresses given by (2.13) to a continuously varying density field. Let us simplify the problem by assuming that shear stresses, τ_{xz} , are zero. Although this is clearly not valid for the entire flow field, symmetry allows us to make this approximation where the deflection of the boundary is at a maximum (near $x = 0$ in (2.13)). We approximate the driving stress, τ_{zz} , as a function of depth by representing the density field as a series of infinitesimally thin layers with density contrast $d\rho$ between them. Then the maximum driving stress, located at $x = 0$, can be written in analogy to (2.13) as:

$$\frac{d\tau_{zz}(z)}{dz} \sim \frac{d\rho(z)}{dz} gZ \quad (2.14)$$

Suppose that density varies with temperature, T , according to:

$$\rho(T) = \rho_m + \rho_m \alpha (T_m - T) \quad (2.15)$$

where ρ_m is the background mantle density, α is the coefficient of thermal expansion, and T_m is the uniform temperature of fluid below the cold upper layer [e.g., *Turcotte and Schubert*, 1982, p. 179]. Integrating (2.14) from $-z_m$, a point at the bottom of the dense layer where $T = T_m$ and the driving stress is zero, to a shallower depth of $-z$ yields:

$$\tau_{zz}(z) \sim \rho_m g \alpha (T_m - T(z)) Z \quad (2.16)$$

where we treat the perturbation amplitude, Z , as constant at all depths in the layer. Because the perturbation Z must go to zero at a rigid surface, we recognize that (2.16) overestimates the stress as z approaches zero.

To relate the driving stresses to the growth of the instability, we use the fact that the vertical strain rate ($\dot{\epsilon}_{zz}$) integrated from $-z_m$ to the surface along the vertical centerline of the sinusoidal perturbation (here $\dot{\epsilon}_{xz} = 0$) is equal to the downward velocity of the perturbation at $z = -z_m$:

$$w(-z_m) = \frac{dZ}{dt} = \int_{-z_m}^0 \dot{\epsilon}_{zz}(z) dz \quad (2.17)$$

This relation should yield the downward velocity at any depth z , not just $-z_m$, but we make this choice because we later relate strain rate to stress, and we wish to include the contribution to the downward velocity from stresses throughout the entire layer.

We proceed assuming a general constitutive relation because we will later consider the case in which $n > 1$. Assuming incompressibility as in (2.2) and that shear strain rates are small near the perturbation's maximum, $\dot{E} \sim \dot{\epsilon}_{zz}$. Then applying (2.5) to (2.17) yields:

$$w = \frac{dZ}{dt} \sim \int_{-z_m}^0 \left(\frac{\tau_{zz}(z)}{B(T(z))} \right)^n dz \quad (2.18)$$

where we allow the rheological parameter, B , to vary with temperature. Defining the driving stress using (2.16), and again assuming that the perturbation amplitude, Z , does not vary with depth, we find:

$$w = \frac{dZ}{dt} \sim \int_{-\infty}^0 \left(\frac{\rho_m g \alpha (T_m - T(z)) Z}{B(T(z))} \right)^n dz \quad (2.19)$$

where we use the fact that the driving stress below the layer is zero to expand the lower integration limit. We can simplify this integral by nondimensionalizing temperature, T' , and the rheological parameter, $B'(T')$:

$$T' = \frac{T - T_s}{T_0} \quad \text{and} \quad B'(T') = \frac{B(T)}{B_m} \quad (2.20)$$

where $T_0 = T_m - T_s$ is the difference between the temperature at depth, T_m , and the surface temperature, T_s , and $B_m = B(T_m)$. Thus, T' varies between 1 at depth and 0 at the surface. We nondimensionalize length according to:

$$z' = z/h \quad (2.21)$$

where h is a length scale associated with the thickness of the unstable layer. Using these nondimensionalizations, we define functions F_n and f_{ab} , according to:

$$F_n = \int_{-\infty}^0 \left(\frac{1 - T'(z')}{B'(T'(z'))} \right)^n dz' = \int_{-\infty}^0 (f_{ab}(z'))^n dz' \quad (2.22)$$

Thus, F_n is the integral through the layer of f_{ab} to the n power. Using this definition of F_n and the nondimensionalizations above, we can simplify (2.19) to:

$$w = \frac{dZ}{dt} = \left(\frac{C'}{n}\right)^n \left(\frac{\rho_m g \alpha T_0}{B_m}\right)^n h F_n Z^n \quad (2.23)$$

where C' is analogous to the super-exponential growth rate C defined by *Houseman and Molnar* [1997], derived with a different approach for a range of constant properties. This expression yields exponential growth of the perturbation amplitude Z if $n = 1$ and super-exponential growth if $n > 1$.

The function f_{ab} in (2.22) weights the negative buoyancy at each point in the thermal structure by the inverse of its viscosity coefficient. For highly temperature-dependent viscosity, the coldest regions, although quite dense, do not yield large values of f_{ab} . Instead, the largest values of f_{ab} occur in relatively warm, less dense regions near the bottom of the thermal structure where viscosity is small. Thus, the weighting offered by f_{ab} accounts for the negative buoyancy of strong material being less important than that of weak material in driving a convective instability. As a result, f_{ab} should scale the contributions of fluid at different depths to the total driving buoyancy. We term F_n , the integral of negative buoyancy divided by viscosity, the “available buoyancy,” because it measures the total negative buoyancy “available” for driving a convective instability. Insofar as F_n properly takes into account the variation of density, viscosity, and temperature with depth in an unstable layer, the dimensionless growth rate in (2.23), C' , should depend only on the wavelength of the initial perturbation. We will test this statement, and thus test the validity of this scaling of the growth rate using the “available buoyancy,” by performing a series of numerical experiments on convectively unstable fluids.

2.2.3 Newtonian Fluids

If $n = 1$ for Newtonian viscosity, (2.23) becomes:

$$\frac{dZ}{dt} = q' \frac{\rho_m g \alpha T_0 h F_1}{2\eta_m} Z \quad (2.24)$$

where C' is replaced by q' . The perturbation, Z , grows exponentially with growth rate:

$$q = q' \frac{\rho_m g \alpha T_0 h}{2\eta_m} F_1 \quad (2.25)$$

If $\Delta\rho = \rho_m \alpha T_0$, this definition of q' is the same as that given in (2.9), except that now our growth rate scales with the parameter F_1 , so q' should vary only with wavelength.

2.2.4 Non-Newtonian Fluids

To analyze non-Newtonian fluids ($n > 1$), we take the time derivative of (2.23):

$$\frac{dw}{dt} = \left(\frac{C'}{n}\right)^n \left(\frac{\rho_m g \alpha T_0}{B_m}\right)^n h F_n n Z^{(n-1)} w \quad (2.26)$$

We eliminate the perturbation size, Z , in favor of the velocity, w , using (2.23):

$$\frac{dw}{dt} = C' \left(\frac{\rho_m g \alpha T_0}{B_m}\right) (h F_n)^{(1/n)} w^{(2n-1)/n} \quad (2.27)$$

Houseman and Molnar [1997] show that integration of (2.27) yields:

$$w = \left[C' \left(\frac{n-1}{n}\right) \frac{\rho_m g \alpha T_0}{B_m} (h F_n)^{(1/n)} (t_b - t) \right]^{\left(\frac{n}{1-n}\right)} \quad (2.28)$$

which is similar to (2.10) and yields super-exponential growth, but includes the “available buoyancy” parameter, F_n . This suggests a nondimensionalization of distance and time of:

$$t' = t \left(\frac{\Delta\rho g h}{B}\right)^n F_n \quad \text{and} \quad z' = \frac{z}{h} \quad (2.29)$$

which is similar to (2.11), but now includes information about how B and ρ vary with depth. Thus, C' should depend only on the perturbation wavelength. Then (2.28) becomes:

$$w' = \left[C' \left(\frac{n-1}{n}\right) (t'_b - t') \right]^{\left(\frac{n}{1-n}\right)} \quad (2.30)$$

which is the same as (2.12), but uses the new nondimensionalization of time. The time t'_b is, of course, a function of the size of the initial perturbation, Z'_0 . By integrating

(2.30), *Houseman and Molnar* [1997] show that:

$$Z'^{(1-n)} = (n-1) \left(\frac{C'}{n} \right)^n (t'_b - t') \quad (2.31)$$

from which we can relate t'_b to Z'_0 by setting $t' = 0$:

$$t'_b = \left(\frac{n}{C'} \right)^n \frac{Z'_0{}^{(1-n)}}{(n-1)} \quad (2.32)$$

2.2.5 The Role of Diffusion of Heat

Diffusion of heat smooths, and thus diminishes, perturbations to an unstable density structure. To quantify thermal diffusion, we compare the rates at which temperature anomalies are advected to those at which they are diffused, in a manner similar to that used by *Conrad and Molnar* [1997]. For conductive transfer of heat in one-dimension:

$$\frac{\partial T}{\partial t} = \kappa \left(\frac{\partial^2 T}{\partial x^2} \right) \quad (2.33)$$

where κ the the thermal diffusivity [e.g., *Turcotte and Schubert*, 1982, p. 154]. We consider thermal diffusion in the horizontal direction because horizontal variations in density grow unstably. Consider perturbations to the background temperature field of the form $T \sim \cos(kx)$. Then (2.33) shows that such perturbations decay exponentially with time as:

$$\frac{\partial T}{\partial t} = -\kappa \frac{4\pi^2}{\lambda^2} T = -q_d T \quad (2.34)$$

which defines the exponential decay rate, q_d .

We wish to compare the rate at which temperature perturbations are diffused to the rate at which they are advected. For the general case of non-Newtonian rheology, we can obtain an instantaneously valid exponential growth rate by comparing (2.23) to the exponential growth equation for $Z(t)$ in (2.8). This gives an exponential growth

rate, q_n of:

$$q_n = \left(\frac{C}{n}\right)^n \left(\frac{\rho_m g \alpha T_0}{B_m}\right)^n h F_n Z^{(n-1)} \quad (2.35)$$

This expression varies with perturbation amplitude, $Z(t)$, so that q_n increases as Z does, yielding the super-exponential growth predicted by (2.28). For a given value of Z , however, it gives an exponential growth rate for advection of temperature perturbations, which we compare to the rate of exponential decay by taking the ratio q_n/q_d . We simplify by ignoring all constants and assume that the fastest growing wavelength scales with the layer thickness, so $\lambda \sim h$. In doing so, we obtain a dimensionless quantity that compares the rate of advection to the rate of thermal diffusion, and thus resembles a Rayleigh number:

$$Ra_n = \left(\frac{\rho_m g \alpha T_0}{n B_m}\right)^n \frac{h^3 Z^{n-1}}{\kappa} F_n \quad (2.36)$$

For Newtonian viscosity, $n = 1$, yielding:

$$Ra_1 = \frac{\rho_m g \alpha T_0 h^3}{2 \kappa \eta_m} F_1 \quad (2.37)$$

which is independent of Z . This ‘‘Rayleigh’’ number, Ra_n , is a measure of the convective instability of a thermal boundary layer, as first described by *Howard* [1964].

2.3 Numerical Experiments

To carry out experiments on both Newtonian and non-Newtonian fluids with different ‘‘available buoyancy,’’ we use the finite element code ConMan, which can solve the coupled Navier-Stokes and energy equations appropriate for thermal diffusion, incompressibility, and infinite Prandtl number [King, Raefsky and Hager, 1990]. This code has been found capable of accurately determining the exponential growth rate of an isothermal Rayleigh-Taylor instability [van Keken *et al.*, 1997]. We initiated convective instability by imposing a temperature field in which cold material overlies warmer material. Because we assign a thermal expansivity α , the colder fluid is

denser, and flows downward into the underlying warm fluid as the instability grows.

Two initial temperature fields are used (Figure 2.1). Conductive cooling of a halfspace, appropriate for the cooling of oceanic lithosphere, yields a temperature profile given by an error function:

$$T(z) = T_s + T_0 \operatorname{erf}(-z/h_c) \quad (2.38)$$

where $h_c = 2\sqrt{\kappa t_c}$ and t_c is the time during which the halfspace has cooled [e.g., *Turcotte and Schubert*, 1982, pp. 163-167]. A linear temperature profile results from conduction of heat across a fixed thickness, h_l :

$$\begin{aligned} T(z) &= T_s + T_0(-z/h_l) & \text{for} & \quad 0 > z > -h_l \\ T(z) &= T_m & \text{for} & \quad z < -h_l \end{aligned} \quad (2.39)$$

To allow instabilities to develop, we perturb the temperature field sinusoidally in the horizontal dimension with a wavelength λ . In particular, we allow the length scales of the thermal profile to vary as:

$$\begin{aligned} h_c(x) &= 2\sqrt{\kappa t_c} \sqrt{1 + p \cos(2\pi x/\lambda)} \\ h_l(x) &= h_l \sqrt{1 + p \cos(2\pi x/\lambda)} \end{aligned} \quad (2.40)$$

where p is a constant that specifies the amplitude of the perturbation. Thus, the thickness of the unstable temperature structure varies between $h\sqrt{1+p}$ and $h\sqrt{1-p}$. This corresponds to a sinusoidal variation in the cooling time, t_c , which has no physical relevance to us, but imposes a smooth perturbation.

So that the unstable layer occupies a constant proportion of the finite element grid, we varied the size of the grid so that its depth is 8.27 times h_c or 7.33 times h_l . The horizontal dimension of the box is determined by the wavelength at which the instability is perturbed, which also scales with h_c or h_l . We use 90 elements in the vertical direction, with 60 elements in the upper half of the box, giving double resolution in the region where the most of the deformation occurs. The number of elements in the horizontal direction is varied so that each element in the upper half

of the box is square.

Boundary conditions on the box are rigid on the top surface, free slip along the two sides, and zero stress along the bottom boundary. Although the Earth's surface is free slip, we choose a rigid top because we wish to study convection beneath the cold upper lithosphere, which is strong and therefore acts as a rigid upper boundary to the fluid beneath it. Furthermore, the free slip boundary condition generally results in flow at wavelengths comparable to the depth of the entire fluid, unless viscosity is highly temperature-dependent [e.g, *Solomatov, 1995; Jaupart and Parsons, 1985*]. In our case, this leads to flow at infinite wavelength because we use a no stress bottom boundary condition. For the Earth, the free-slip boundary condition results in plate-scale flow, which is not under study here. Nevertheless, we do perform a few calculations with a free slip upper boundary for comparison.

The no stress bottom boundary condition permits fluid to flow in and out of the bottom boundary so that material is not constrained to circulate within the box, which could impede flow. The box is sufficiently deep, however, that the base of a growing instability, defined by the location of the $T' = 0.9$ isotherm, only penetrates the top 30% of the box before the instability begins detach from the overlying layer. To see how this bottom boundary may effect our results, we tried imposing zero horizontal velocity on the bottom boundary while maintaining free flow of material in the vertical direction. This boundary condition produces unstable growth that is less than $10^{-5}\%$ slower than it is for the no stress boundary condition, indicating that our choice of the latter does not significantly speed unstable growth.

Because we are studying the time-dependence transient phenomena, the accuracy of our time stepping routine is important. We use an explicit predictor-corrector algorithm, which should be accurate to second-order [*Hughes, 1987, pp. 562-566*]. After several tests, we chose a time step that is one tenth that of the dynamically chosen Courant time step. Increasing the temporal resolution further produced measured growth rates that were larger by only a few percent. Because we do not hope to be able to measure growth rates to better than one, and possibly two, significant figures, this degree of error was deemed acceptable.

We allow density, ρ , to vary with temperature according to (2.15). As a result, density, and thus the buoyancy that drives the instability, varies with depth (Figure 2.1). The temperature dependence of the rheological strength parameter, B , is generally given as:

$$B(T) = B_0 \exp\left(\frac{E_a}{nRT}\right) \quad (2.41)$$

where B_0 is an initial value of B , E_a is an activation energy, R is the universal gas constant, and T is temperature in Kelvins [e.g., *Kohlstedt, Evans, and Mackwell, 1995*]. We can define B_0 such that $B(T_m) = B_m$, from which we approximate (2.41) as:

$$B(T) = B_m \exp\left(\frac{E_a(T_m - T)}{nRT_m^2}\right) \quad (2.42)$$

If we define a variable $r = \exp(E_a T_0 / nRT_m^2)$, we can rewrite (2.42) as:

$$B(T) = B_m \exp\left(\ln(r) \frac{T_m - T}{T_0}\right) \quad (2.43)$$

Thus, the parameter r describes how strongly B varies with temperature. In addition, because $\eta(T_s) = r\eta_m$, r represents the total variation in B across the fluid.

By increasing r , we increase the strength of the cold, dense portions of the unstable density structure and thus decrease their ability to participate in a convective downwelling. The variation of the function f_{ab} , as given by (2.22), with depth (Figure 2.2) provides a measure of the relative contributions of each level in the unstable density profile to the convective instability as a whole. For constant B ($r = 1$), the greatest contribution to the instability occurs in the coldest, densest regions at the surface of the layer. As this cold material is strengthened, however, by an increase in r , the greatest contribution occurs deeper in the layer, where material is sufficiently warm to be weak enough to participate in the downwelling. For the most strongly temperature-dependent viscosity ($r = 1000$), only the bottom portion of the dense layer can contribute. This region is thinner for the linear profile than the error-function profile, because the latter contains more warm material.

We argue above that the integral of the n^{th} power of the contribution function,

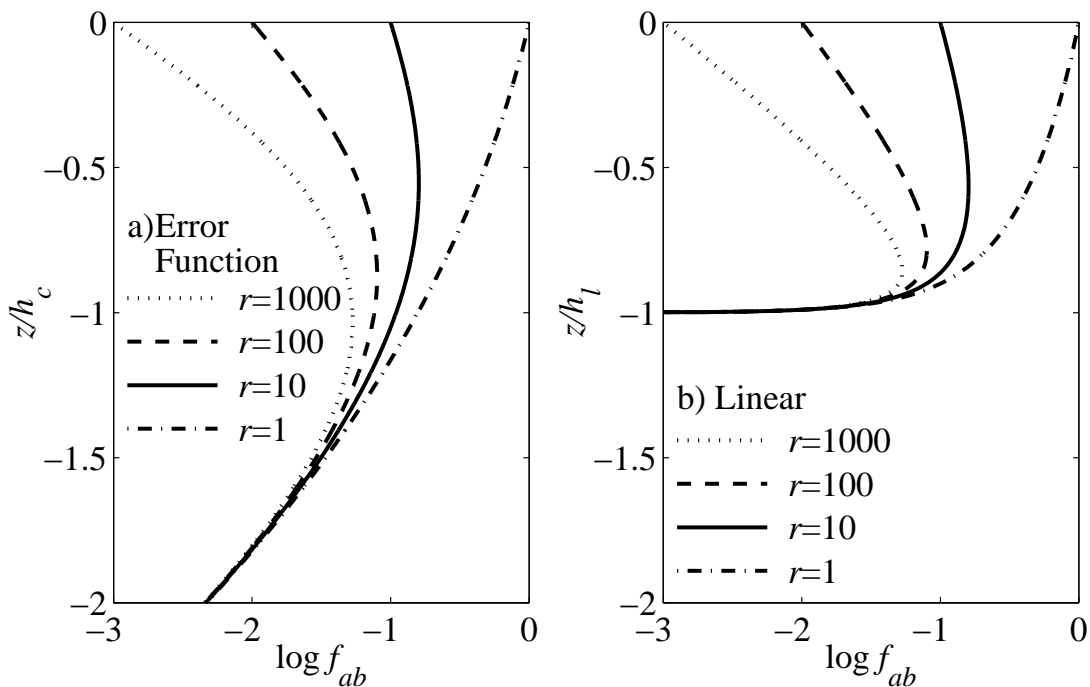


Figure 2.2: Plot of the log of the “available buoyancy” function, f_{ab} , given by (2.22) as a function of dimensionless depth for the (a) error-function and (b) linear temperature profiles. For each profile, $f_{ab}(z')$ is given for four temperature dependences of viscosity, using values of r of 1, 10, 100, and 1000 in (2.43). The decrease of f_{ab} with increasing viscosity contrast is shown by the decrease of f_{ab} as z' approaches zero, as r increases. The integral of f_{ab}^n with depth gives the total “available buoyancy,” F_n (Figure 2.3). For $n > 1$, f_{ab}^n can be represented by multiplying the horizontal axis by n .

f_{ab}^n , should scale with the growth rate of the instability. We calculated $F_n(r)$ by numerically integrating the curves given in Figure 2.2 for both error-function and linear temperature profiles, and for $n = 1$ and $n = 3$ (Figure 2.3). Because $f_{ab} \leq 1$, $F_3 < F_1$ for all r , and F_3 decreases significantly faster than F_1 with increasing r (Figure 2.3). The linear temperature profile exhibits smaller values of F_n than does the error-function profile, especially for large r , because less warm material is available to participate in the instability (Figure 2.2).

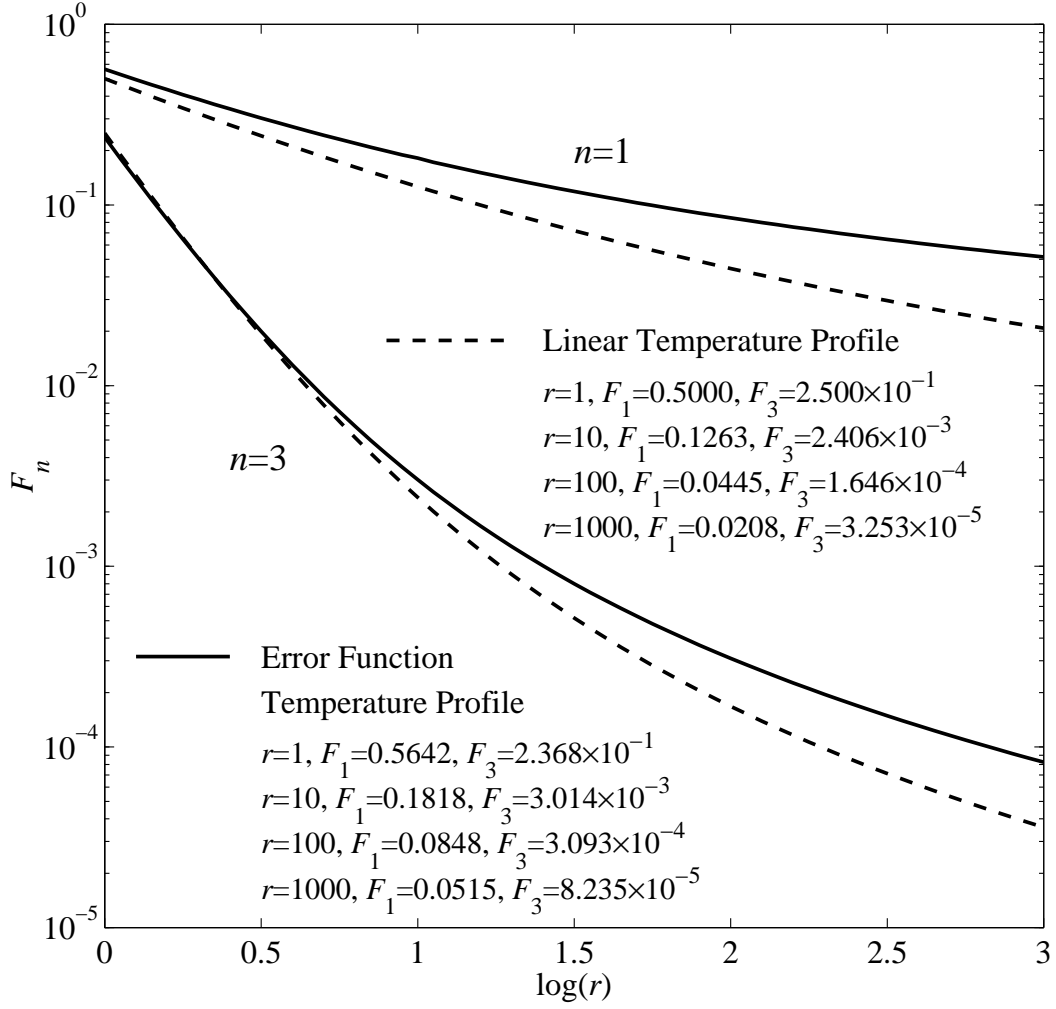


Figure 2.3: The total available buoyancy, F_n , as a function of $\log r$ for both the error-function and linear temperature profiles, and for $n = 1$ and $n = 3$. F_n is calculated by integrating f_{ab} (Figure 2.2) according to (2.22). As the temperature dependence of viscosity increases with increasing r , more of the negative buoyancy becomes unavailable for driving a convective instability because of its increased strength. This is shown by the decrease of F_n with r .

2.4 Results for Newtonian Viscosity

We first examine the role of temperature-dependent Newtonian viscosity on the exponential growth of convective instability for an error-function temperature profile (Figure 2.4). Increasing the temperature dependence of viscosity decreases the amount of material that participates in the instability. For example, only the bottom isotherm ($T' = 0.9$) shows significant deflection at large amplitudes for $r = 1000$ (Figure 2.4d), while nearly the entire unstable layer participates in the downwelling for $r = 1$ (Figure 2.4a). For each value of r , the shallowest significantly deflected isotherm lies near the maximum in the corresponding profile of f_{ab} in Figure 2.2a. Thus, the curves in Figure 2.2 appear, at least qualitatively, to represent the regions of the dense layer participating in the convective instability. The exception is for $r = 1$. The rigid boundary condition permits no deflection at the surface, but $f_{ab}(r = 1)$ has a maximum there (Figure 2.2).

When made dimensionless without scaling by “available buoyancy,” the time for an instability to reach a given amplitude increases as the temperature dependence of viscosity increases (Figure 2.4). We can quantify this effect by calculating a dimensionless growth rate, as for a Rayleigh-Taylor instability, for each viscosity profile. To do this, we measure the downward speed, w , of the $T' = 0.9$ isotherm as a function of time. Because this isotherm is near the bottom of the unstable layer, its speed gives us a measure of the growth of the entire instability. We nondimensionalize (2.8) using (2.11), which gives:

$$\ln w'' = \ln w_0'' + q'' t'' \quad (2.44)$$

where w_0'' is the initial dimensionless velocity. If growth is exponential, a plot of $\ln w''$ versus t'' should then yield a linear relationship with slope equal to q'' . The initially linear slopes shown in Figure 2.5a for the four cases shown in Figure 2.4 indicate that the instability begins its growth exponentially. Following the initial exponential growth stage, the instabilities accelerate slightly as non-linear effects become more important at large amplitudes. This behavior is also observed by *Houseman and Molnar* [1997] who attribute the acceleration in part to the selection of the fastest

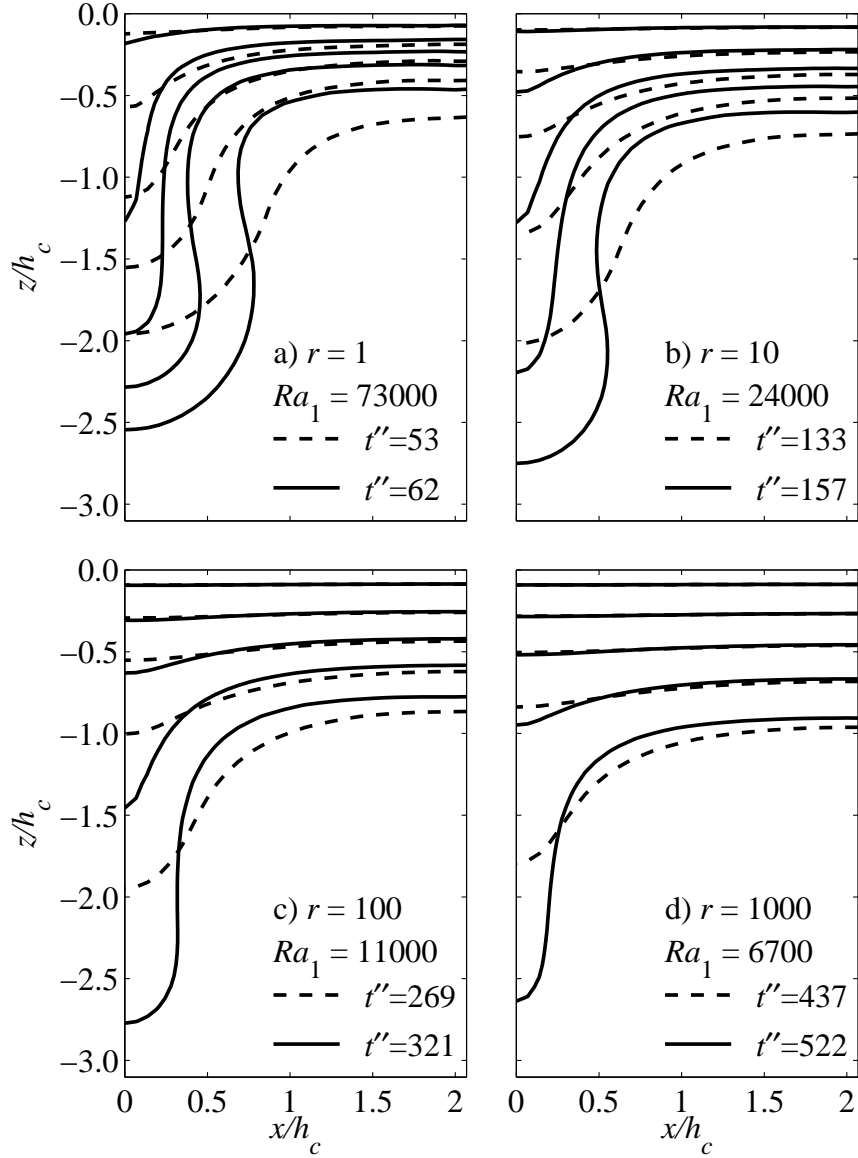


Figure 2.4: Temperature profiles showing the growth of a convective instability from an initially error-function temperature profile perturbed using (2.40) with $p = 0.04$ and $\lambda' = \lambda/h_c = 4.14$. Shown are isotherms for T' of 0.1, 0.3, 0.5, 0.7, and 0.9, with the lower temperatures closer to the surface. Sets of profiles for four values of r of 1, 10, 100, and 1000 are shown in parts (a) through (d). In each part, two sets of isotherms show different stages of growth. We chose profiles for which the maximum depth to the $T' = 0.9$ isotherm was between 1.5 and $2.0h_c$ (dashed lines) and between 2.5 and $3.0h_c$ (solid lines). The times for each are given and are nondimensionalized using (2.11) without the “available buoyancy.” It is clear that the profiles with more strongly temperature dependent viscosity require more time to reach a given amplitude and remove a smaller amount of material.

growing wavelength at large amplitudes. Because we allow instabilities to grow to very large amplitudes, this non-linear phase is followed by a period in which growth of the instability begins to taper off and the downwelling plume approaches a constant velocity. When the instability detaches from the unstable layer, it should reach a “terminal” velocity, a condition described approximately by Stokes flow, the descent of a heavy sphere in a viscous fluid [e.g., *Turcotte and Schubert*, 1982, pp. 263-268].

Growth rates, q'' , show a strong dependence on the temperature dependence of viscosity, with larger r yielding slower growth. When time is nondimensionalized using (2.29) to include the “available buoyancy” (Figure 2.5b), however, the four curves nearly collapse onto a single curve, with approximately equal dimensionless exponential growth rates, q' . This indicates that the “available buoyancy” scales the affect of the temperature dependence of viscosity. We attribute the relatively low dimensionless growth rate for $r = 1$ to the influence of the rigid top boundary of the fluid. As discussed above, this condition does not permit this instability to utilize the significant “available buoyancy” near the surface of the layer for $r = 1$ (Figure 2.2), so the scaling with F_1 overestimates the amount of dense material that participates in the instability. For $r > 1$, there is little contribution to the “available buoyancy” from the surface because the material is strong there, and F_1 more accurately represents the amount of material available for driving a convective instability.

Growth rates nondimensionalized without “available buoyancy” depend on both the temperature dependence of viscosity and on the wavelength of the initial perturbation (Figure 2.6a). When scaled by “available buoyancy,” however, the three curves for $r > 1$ approximately collapse onto a single curve that depends only on wavenumber (Figure 2.6b). There remains a difference at short wavelengths ($k' > 2$), some of which is due to the presense of the rigid lid, as discussed above. Similar calculations using a free slip upper boundary condition (Figure 2.7) show that for short wavelengths, the “available buoyancy” scaling works slightly better with a free top (compare Figures 2.6b and 2.7). Growth rates at long wavelengths (small k') are not properly scaled if top boundary slips freely because in this case the preferred wavelength scales with the depth of the box and not the depth of the unstable layer. For

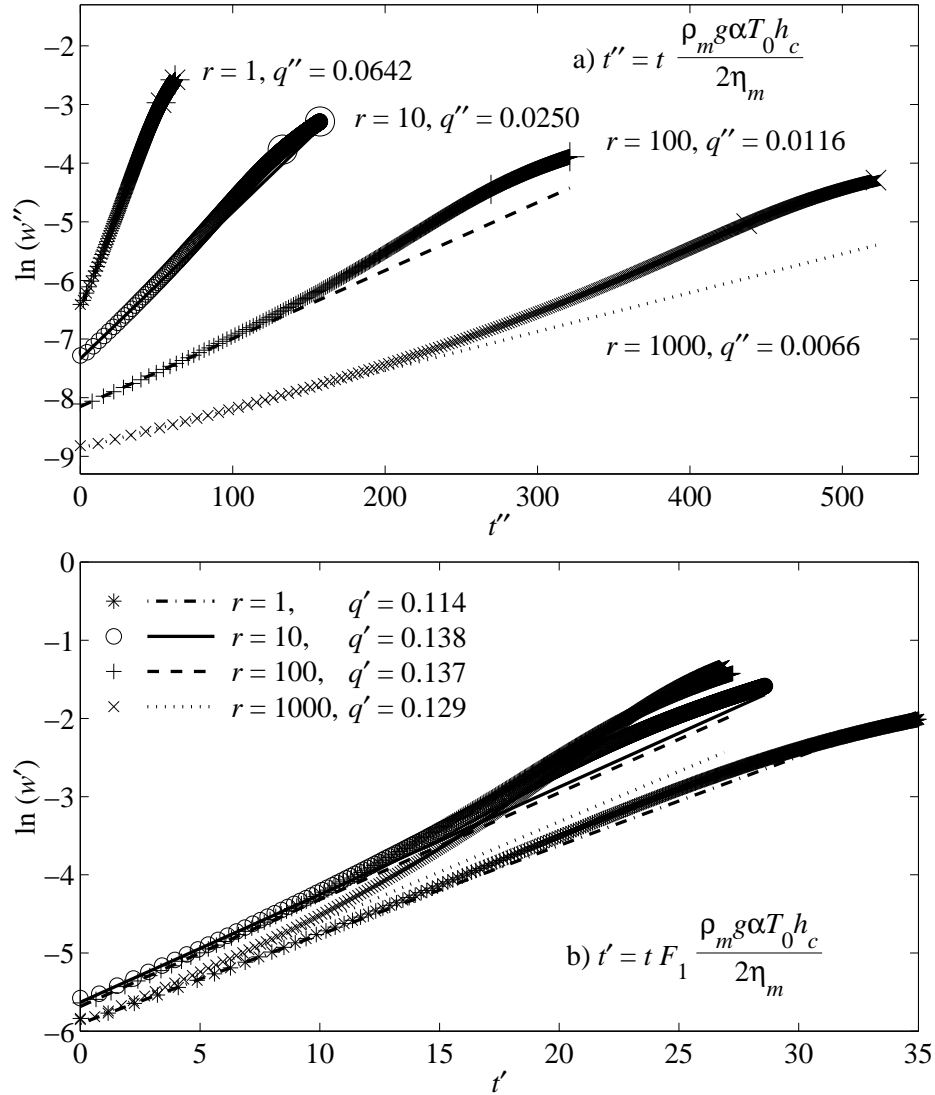


Figure 2.5: Plots of $\ln(w'')$ or $\ln(w')$, the natural log of the dimensionless downward speed of the $T' = 0.9$ isotherm at $x' = 0$, versus dimensionless time, t' or t'' , for the four convective instabilities profiled in Figure 2.4. Time is nondimensionalized using (2.11) in (a), indicated by double primes, and by (2.29) in (b), indicated by single primes. Thus, (b) scales rates with “available buoyancy,” but (a) does not. For each value of r , the symbols represent output from finite element calculations, and lines represent linear fits to the initial slope, the value of which is the dimensionless growth rate, q' or q'' . The growth rates scaled by “available buoyancy” are nearly independent of r , showing that this scaling accounts for the temperature dependence of viscosity. The big symbols indicate the times for which temperature profiles of the instability are given in Figure 2.4.

the nearly isoviscous cases of $r = 1$ and $r = 10$, this allows the longest wavelengths to grow most rapidly (Figure 2.7), but if viscosity is highly temperature-dependent, growth rates decrease with wavelength, as they do for a rigid lid (compare $r = 1000$ curves in Figures 2.6b and 2.7). Thus, the “available buoyancy” does a better job of scaling the temperature dependence of viscosity if the upper boundary is free slip, but only for short and intermediate wavelength perturbations.

For the rigid top, we also attribute some of the unscaled differences in q' at large wavelength (Figure 2.6b) to the decrease of the wavelength of maximum growth rate with increasing r . As the viscosity becomes more temperature-dependent, the thickness of the unstable layer that participates in the instability decreases. This thickness should scale with the dominant wavelength [Conrad and Molnar, 1997; Molnar, Houseman and Conrad, 1998], so that the maximum value of q'' or q' should occur at shorter wavelengths for larger r , as can be seen in Figure 2.6b. As a result, q' at short wavelengths is smaller for smaller values of r .

Similar calculations using a rigid top and an initially linear temperature profile (Figure 2.8) yield wavelengths of maximum growth rate that depend on r more than they do for an error-function temperature profile (Figure 2.6). We attribute this to the presence of more warm material, and thus more “available buoyancy,” near the bottom of the error-function profile than the linear profile (Figure 2.2). Because this material always participates in an instability, the effective thickness of the unstable part of the layer is less variable for the error-function profile than it is for the linear profile. Thus, the effective thicknesses of the “available buoyancy” curves, f_{ab} , in Figure 2.2 depend more on r for the linear profile. Because the wavelength of maximum growth rate should scale approximately with this thickness, its values show a greater variation for the linear temperature profile.

The “available buoyancy” scaling of the growth rate appears to account for the temperature dependence of viscosity in the results for the linear temperature profile (Figure 2.8). Because the wavelength of maximum growth rate varies with r , the curves for different r do not fall together when scaled with the “available buoyancy” (Figure 2.8b). The value of the maximum growth rate, however, is the same for all

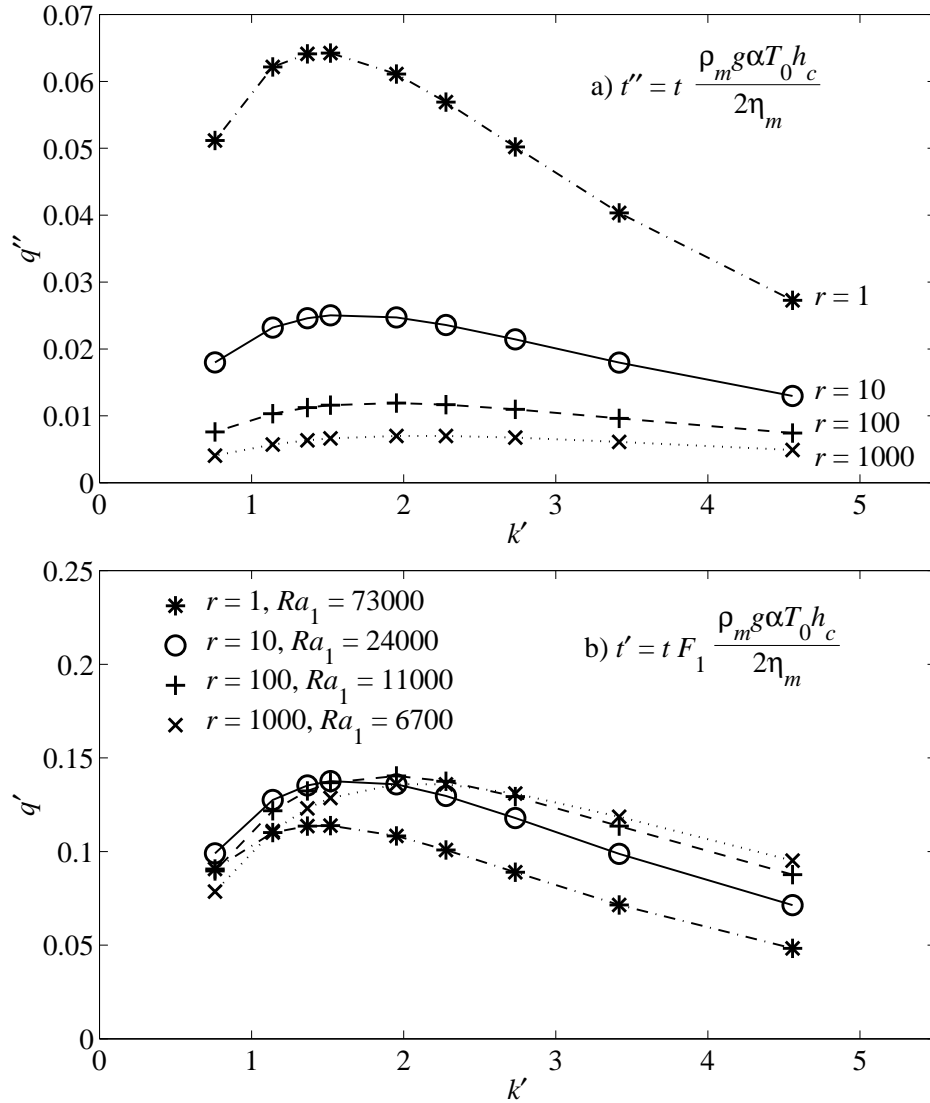


Figure 2.6: Plots of dimensionless growth rate, q'' or q' , versus dimensionless wavenumber, $k' = 2\pi/\lambda'$, with time and length scaled using (2.11) in (a) and (2.29) in (b). Thus, (b) scales rates with the “available buoyancy.” We used an error-function initial temperature profile perturbed using (2.40) with $p = 0.04$.

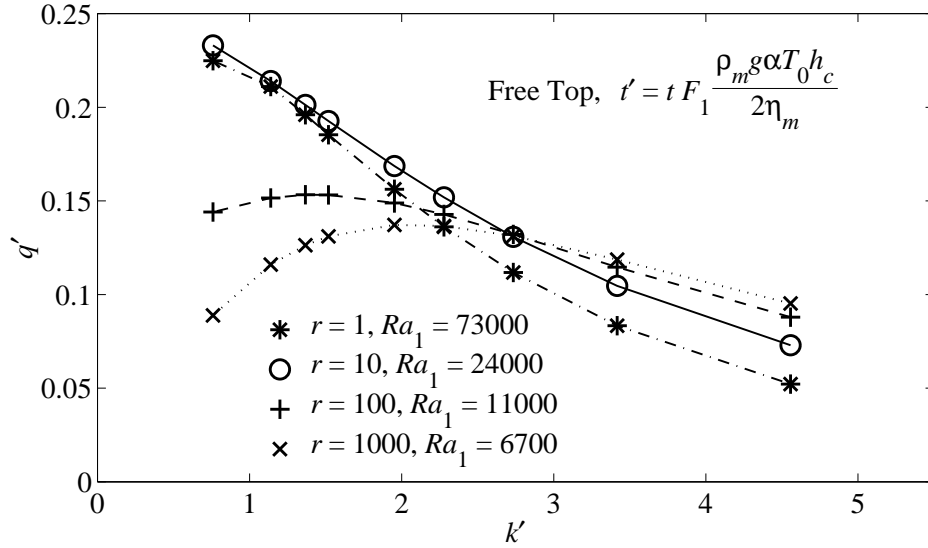


Figure 2.7: Similar to Figure 2.6b, but for free slip boundary conditions on the top surface, again using the “available buoyancy” to scale time. A comparison to Figure 2.6b shows that for short wavelengths ($k' > 2$), the “available buoyancy” scaling accounts for the temperature dependence of viscosity slightly better if the upper boundary condition is free slip. At long wavelengths ($k' < 2$), however, the “available buoyancy” scaling shown here breaks down because, for free slip, the longest wavelengths grow most rapidly, except for large r .

$r > 1$. (For $r = 1$, the presence of the rigid surface causes this scaling to overestimate the actual growth rate, as discussed above.) Furthermore, the maximum value of q'' for the linear temperature profiles is about 0.18 (Figure 2.8b), which is only about 20% larger than the maximum value of about 0.14 found for the error-function temperature profile (Figure 2.6b). This agreement is more impressive when we recall that for $r = 100$ and $r = 1000$, the “available buoyancy” scaling differs by a factor of approximately two between the linear and error-function temperature profiles (Figure 2.3). The agreement of growth rates for different temperature profiles suggests that the “available buoyancy” scaling provides a dimensionless growth rate that is independent of the functional form of the initial temperature profile.

If viscosity is Newtonian ($n = 1$), growth rates for a Rayleigh-Taylor instability can be predicted from linear theory. We use the analysis of *Conrad and Molnar* [1997] to predict growth rates for an unstable layer with a linear temperature profile

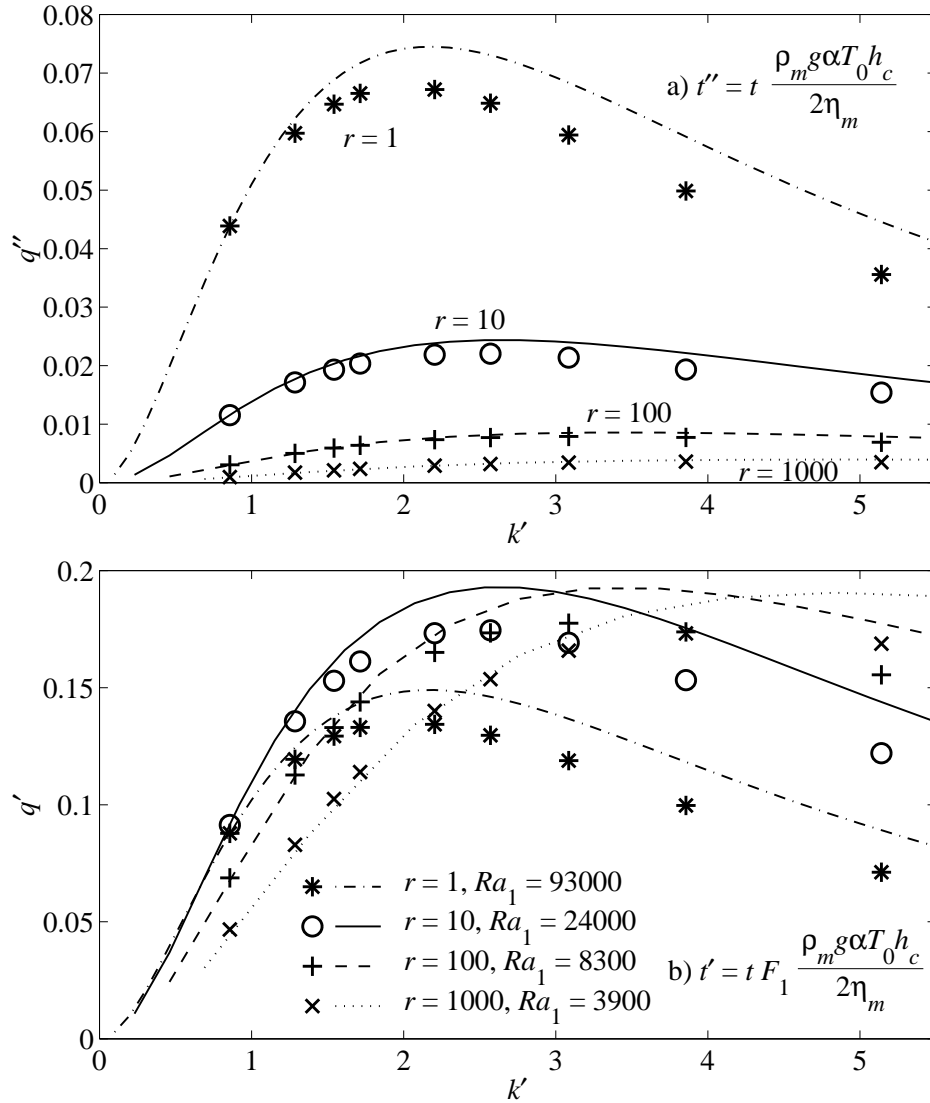


Figure 2.8: Similar to Figure 2.6, for an initially linear temperature profile, perturbed using (2.40) with $p = 0.04$. In this case, however, symbols show growth rates estimated from the finite element calculations and lines show growth rates predicted by Rayleigh-Taylor linear theory, as given by *Conrad and Molnar* [1997].

and exponentially varying viscosity. Such calculations yield growth rates that agree to within 10% of those measured here (Figure 2.8). The greatest deviation occurs at short wavelengths, but tests show that increasing the spatial resolution of the finite element grid reduces this disagreement. The agreement between Rayleigh-Taylor theory and our calculations, which include thermal diffusion, indicates that the convective instability approximates a Rayleigh-Taylor instability, at least for the high values of Ra_1 used here. The agreement also indicates that ConMan accurately simulates the convective instability.

We investigated the conditions for the stability of a cold, dense layer by measuring q' for different values of the stability parameter, Ra_n (Figure 2.9). We calculated growth rates for a linear temperature profile and $k' = 3.1$, chosen because it is near the maximum of the q' versus k' curves for $r = 10, 100, \text{ and } 1000$ (Figure 2.8b). The three values of $q'(Ra_1)$ for these values of r differ from one another by less than 10%, when dimensionless growth rates are calculated using the “available buoyancy.” For large values of Ra_1 , q' is approximately equal to 0.18, as we observed in Figure 2.8b. When Ra_1 is less than about 500, growth is slowed, and for Ra_1 less than about 50, growth is stopped altogether. This decrease in q' is due to the suppression of temperature perturbations by thermal diffusion as Ra_1 decreases.

The ability of thermal diffusion to suppress unstable growth should vary with wavelength because small wavelength perturbations are most susceptible to smoothing by thermal diffusion in the horizontal direction. This is evident in Figure 2.10, where, for large k' , growth is stopped or significantly slowed for the smallest values of Ra_1 . At longer wavelengths, however, growth rates for this same value of Ra_1 become greater than those of the larger Ra_1 calculations. Long wavelength perturbations are less prone to smoothing by horizontal thermal diffusion, and for sufficiently small Ra_1 , they appear to grow more rapidly than those with larger Ra_1 . We attribute relatively high dimensionless growth rates at long wavelengths also to thermal diffusion, but in the vertical direction. If the layer cools sufficiently during advective growth, its thickness and the amount of unstable material will increase so that the instability proceeds with more “available buoyancy” than the initial conditions suggest. This

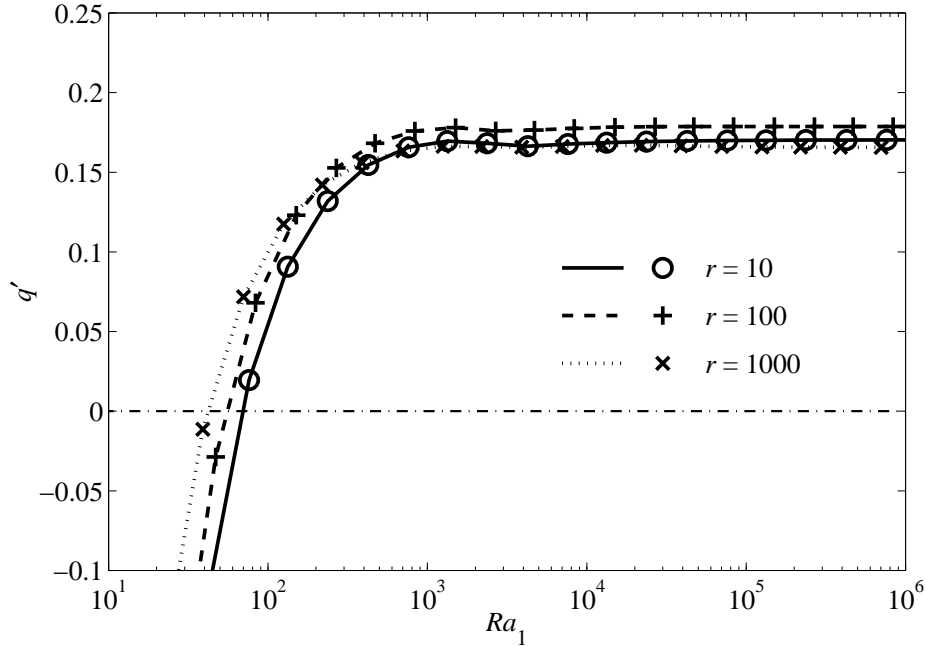


Figure 2.9: Plot showing how the dimensionless growth rate, q' , varies with the stability parameter, Ra_1 , for a layer with Newtonian viscosity ($n = 1$) and for r of 10, 100, and 1000. Scaling is with the “available buoyancy,” as given by (2.29). A linear temperature profile, perturbed using (2.40), $\lambda' = \lambda/h_l = 4.07$, and $p = 0.04$ giving $Z'_0 = 1.98\%$, was used in each case, and we varied Ra_1 by varying η_m .

causes growth rates that are scaled by the original amount of “available buoyancy” to increase.

2.5 Results for Non-Newtonian Viscosity

We performed several runs using a non-Newtonian viscosity with power law exponent $n = 3$, and a variable initial perturbation size. We use an initial perturbation to an error-function temperature profile given by (2.40) in which t_c varies by 20%, giving a maximum downward perturbation of $Z_0 = 0.0954h_c$. The results (Figure 2.11) are qualitatively similar to those presented for Newtonian rheology in Figure 2.4 in that a smaller fraction of the dense layer is removed in a longer period of time for layers with more highly temperature-dependent rheology. The retarding by a highly temperature-dependent rheology, however, is more pronounced for non-Newtonian

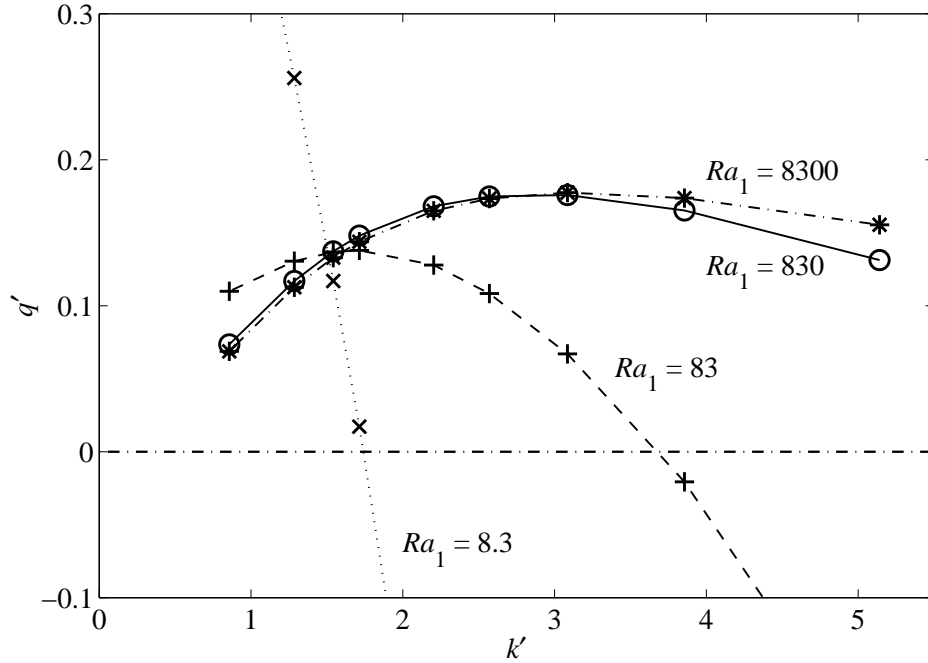


Figure 2.10: Plots of dimensionless growth rate, q' , versus dimensionless wavenumber, $k' = 2\pi/\lambda'$, for an initially linear temperature profile, perturbed using (2.40) and $p = 0.04$. All curves use $r = 100$, and Ra_1 is varied by varying η_m . Time is scaled using (2.29) to include the “available buoyancy.”

viscosity than it is for Newtonian viscosity. For example, the Newtonian runs with $r = 1000$ (Figure 2.4d) take about 8 times as long to reach the same amplitude as the $r = 1$ runs (Figure 2.4a), when time is nondimensionalized without the “available buoyancy”. This ratio is closer to 8^3 , or 500, for the non-Newtonian cases (Figures 2.11a and 2.11d). Thus, for $n = 3$, non-Newtonian viscosity approximately cubes the effects of temperature dependence of B . This is an indication that our definition of the “available buoyancy” in (2.22), where $F_n \sim f_{ab}^n$, may be applicable for $n > 1$.

Some of the temperature contours show a deflection toward the surface near the left edge of the calculations shown in Figure 2.11, indicating that temperatures do not always increase away from the center of the instability. This observation is somewhat surprising because it is not what we found for Newtonian rheology (Figure 2.4). One explanation could be numerical error. *Travis et al.* [1990] show that errors in the

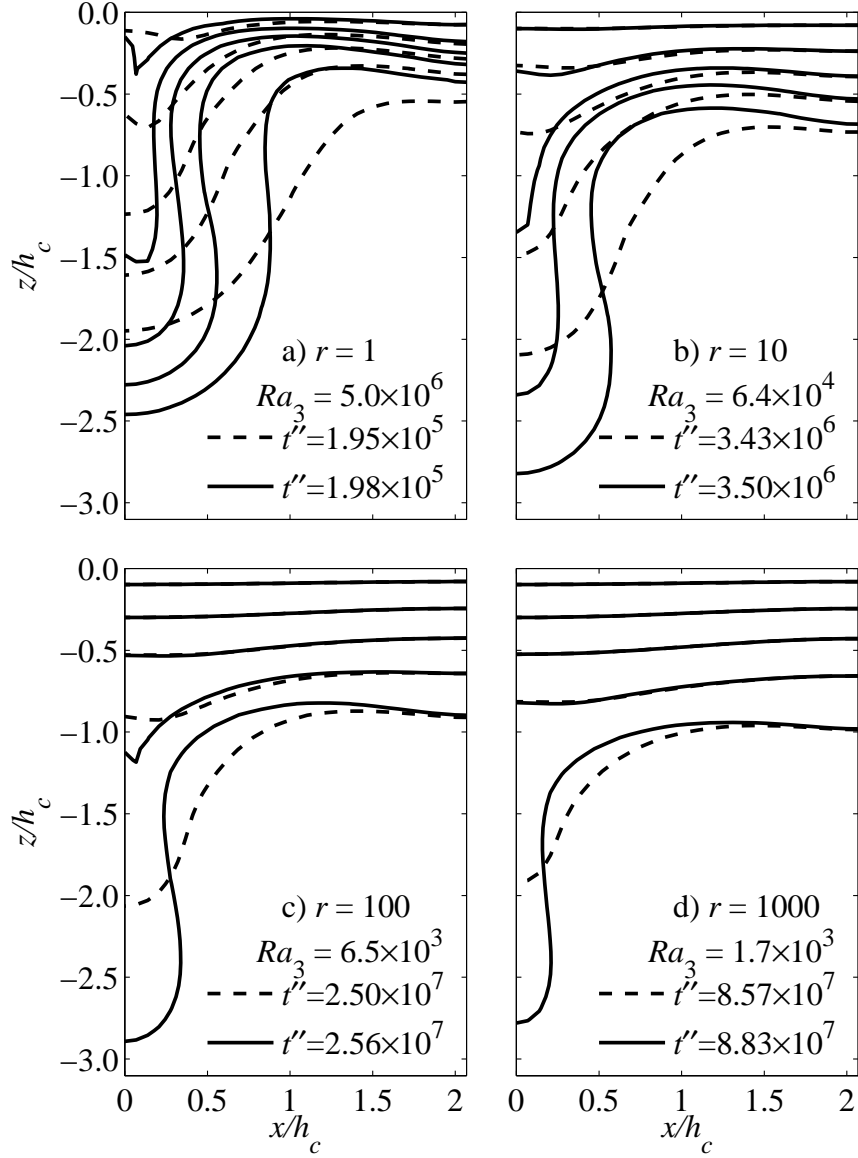


Figure 2.11: Similar to Figure 2.4, but for temperature profiles showing the growth of a convective instability in a non-Newtonian fluid ($n = 3$) from an initially error-function temperature profile that is perturbed using (2.40) with $p = 0.2$ and $\lambda' = \lambda/h_c = 4.14$. The times for both stages of the instability are given, and are scaled using (2.11), without the “available buoyancy.”

temperature field tend to be maximized near the stagnating regions of a finite-element grid. If numerical error is a problem, however, it is not diminished by increasing the spatial resolution of the finite element grid or by allowing the surface node nearest the corner to move freely in the horizontal direction to prevent “grid locking.” Furthermore, other numerical codes produce similar results [*U. Christensen, personal communication, 1998*]. Another explanation could be related to the stress dependent viscosity, which would tend to increase the effective viscosity of the stagnant corner region due to the low strain rates there. The effective viscosity of the material just to the side of the stagnant corner, however, should decrease due to the presence of significant strain rates that advect temperature contours around the corner from the side. For increasingly temperature-dependent viscosity, the stagnant corner becomes less pronounced, because it is not associated with the rigid lid, and deeper, because the zone of active deformation is shifted downwards (Figure 2.11). In any case, the net effect of this phenomenon, which represents less than a 10% difference in temperature across a small portion of the entire downwelling region, should be small.

The runs with non-Newtonian viscosity show a greater acceleration of the instability with increasing time than do the Newtonian results. For Newtonian viscosity, about 15% of the total time is spent between the two temperature profiles shown in Figure 2.4, compared to between 1.5 and 3% for runs with non-Newtonian viscosity (Figure 2.11). Clearly growth for non-Newtonian viscosity accelerates faster than the exponential growth we observe for Newtonian viscosity, as *Houseman and Molnar [1997]* demonstrate for the Rayleigh-Taylor instability. To test *Houseman and Molnar’s [1997]* scaling law, we again determine the velocity of the $T' = 0.9$ isotherm as a function of time for the four calculations contoured in Figure 2.11. According to (2.12), a plot of $w''^{(-2/3)}$ as a function of dimensionless time, t'' , should be linear, with slope equal to $-2C''/3$ and a time intercept of t_b'' . Because t_b'' varies by orders of magnitude with changes in r (Figure 2.11), we rescale both axes by dividing by t_b'' (Figure 2.12a). Thus, all curves have the same time intercept at $t''/t_b'' = 1$, and their relative slopes can be compared easily.

The relationships between $w''^{(-2/3)}$ and t'' are clearly linear for all r (Figure 2.12a),

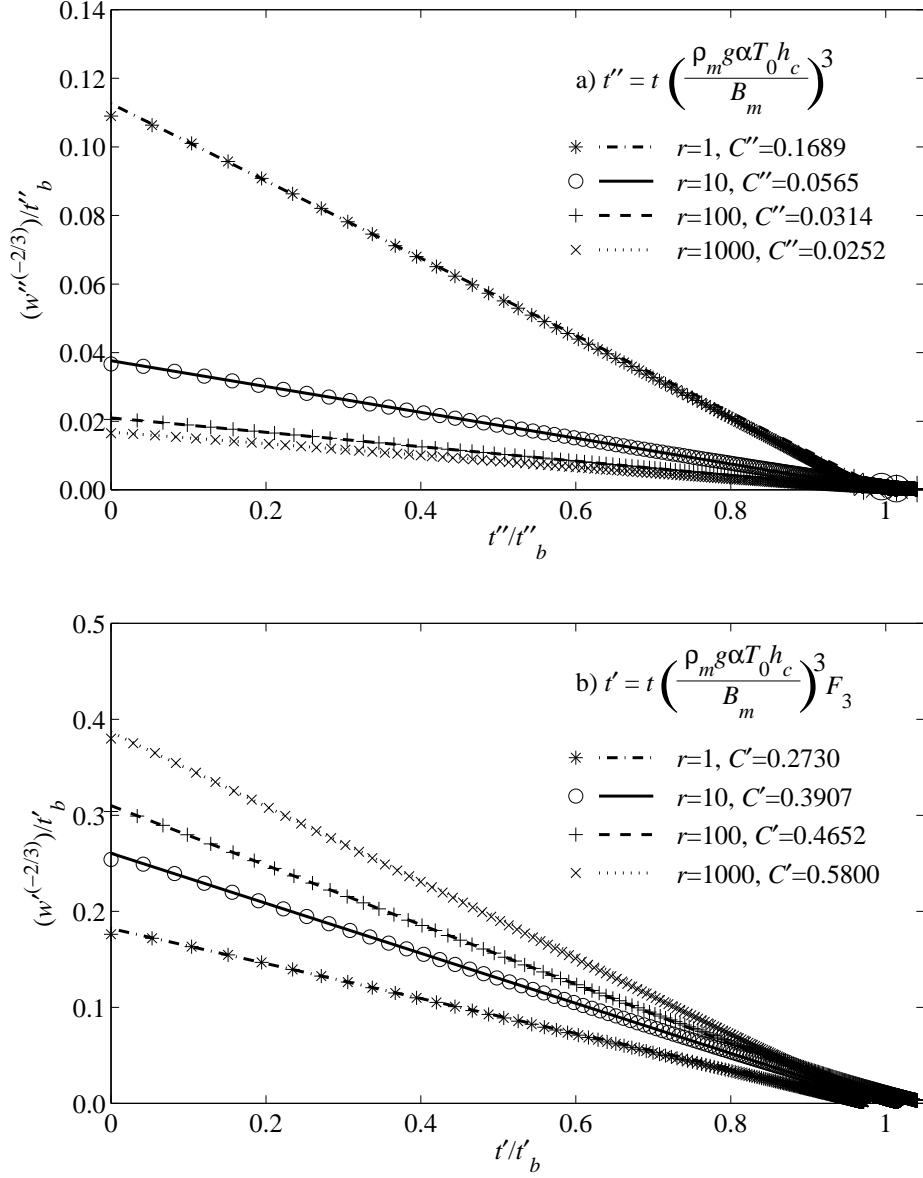


Figure 2.12: Plots of (a) $w''^{(-2/3)}/t''_b$ versus t''/t''_b , where double primes indicate a scaling of time without the “available buoyancy” using (2.11) and of (b) $w'^{(-2/3)}/t'_b$ versus t'/t'_b , where single primes indicate a scaling of time with the “available buoyancy” using (2.29). We define w'' or w' as the downward speed of the $T' = 0.9$ isotherm at $x' = 0$, for the four convective instabilities profiled in Figure 2.11, and big symbols in (a) represent times that are profiled there. We scale each curve with the time t''_b or t'_b so that the four curves can be compared more easily. The linear relationships shows that the instabilities grow super-exponentially, as predicted by *Houseman and Molnar* [1997]. The lines show linear fits to the initial portion of the numerical results (symbols), and we estimate values of C'' and C' from the slope of this line.

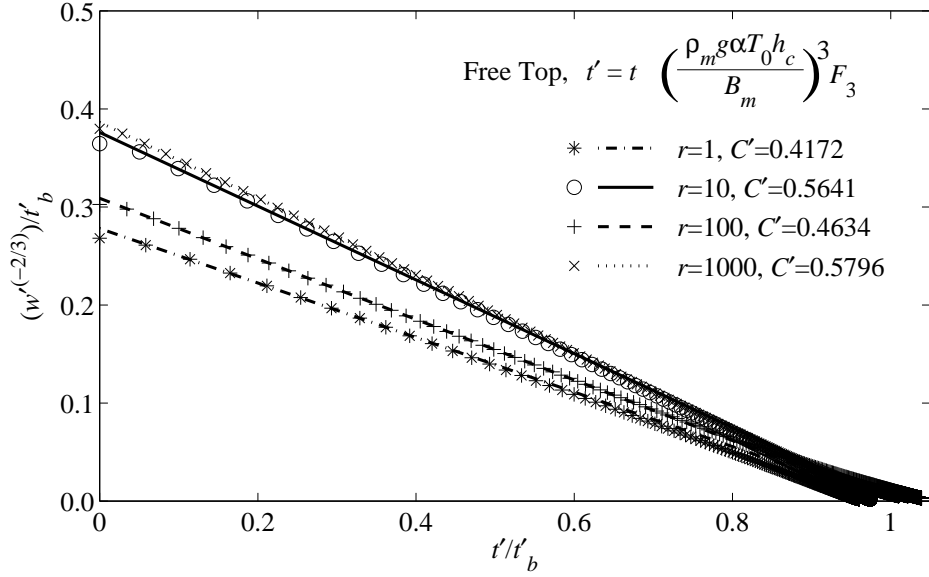


Figure 2.13: Similar to Figure 2.12b, but for free slip boundary conditions on the top surface, again using the “available buoyancy” to scale time. A comparison to Figure 2.6b shows that the “available buoyancy” scaling better accounts for the temperature dependence of viscosity if the upper boundary condition is free, rather than rigid.

and their slopes yield values of C'' that decrease by a factor of about 7 as r increases from 1 to 1000 (Figure 2.12a). When time is nondimensionalized using (2.29) to include the “available buoyancy,” and $w'^{(-2/3)}$ is plotted versus t' (Figure 2.12b), the discrepancy between the slopes for different r is improved, but $C''(r = 1)$ and $C''(r = 1000)$ still differ by about a factor of two. This scatter is considerably improved to within about 15% of its mean value if the upper boundary condition is free slip (Figure 2.13), but for the rigid top, large scatter is observed at all wavelengths (Figure 2.14). As we found for Newtonian viscosity, a rigid surface boundary condition causes the “available buoyancy” scaling to overestimate the rate of growth for the isoviscous case ($r = 1$), presumably because it includes a contribution from dense material near the rigid surface that can not participate in the instability. For $r > 1$, estimates of C' fall within about 20% of their median value of $C'(r = 100) = 0.47$ (Figures 2.12b and 2.14b). For an initially linear temperature profile, maximum values of C' are between 0.4 and 0.5 for all $r > 1$ (Figure 2.15b). The isoviscous case,

$r = 1$, again yields values of C' that are smaller than those for $r > 1$. For non-Newtonian viscosity and a rigid top, the scaling of the temperature dependence of viscosity using the “available buoyancy” is less impressive than it was for Newtonian viscosity, but it still provides a useful method of approximating super-exponential growth rates, and appears to be somewhat independent of the functional form of the initial temperature profile.

Linear theory can not provide predictions of super-exponential growth rates, but we can compare our calculations for the linear temperature profile to those of previous numerical studies of the Rayleigh-Taylor instability. For $r = 1$, *Houseman and Molnar* [1997] give a maximum value of $C'' = 0.37$ for $n = 3$ and a linear density profile over an inviscid halfspace, where we have divided by two to make their nondimensionalization agree with ours, and by $2^{(1/3)}$ to account for the difference in their definition of \dot{E} . This is nearly a factor of two larger than the maximum value we measure of $C = 0.21$ (Figure 2.15a). Some (maybe half) of this discrepancy is expected because we do not use an inviscid lower halfspace. We have adjusted estimates of C'' by *Molnar, Houseman, and Conrad* [1998] for the Rayleigh-Taylor instability of a layer with B decreasing exponentially and density decreasing linearly over a halfspace of constant B by dividing by a factor of $(\ln r)^{(n+1)/n}$ to make them agree with our nondimensionalization. These adjustments yield $C'' = 0.096$ for $r = 10$ and $C'' = 0.040$ for $r = 100$. Our measurements of $C'' = 0.064$ and $C'' = 0.026$ (Figure 2.15a) are about 70% those of *Molnar, Houseman, and Conrad* [1998]. This discrepancy may be numerical, but could also be due to the different density structures at the bottom of the layers; for *Molnar, Houseman, and Conrad* [1998], there is no diffusion of heat, but with such diffusion, density, and hence mass, is redistributed before significant growth occurs. Moreover, such a redistribution occurs where viscosity is lowest, and thus at a level that affects the “available buoyancy” most. Thus, perhaps we should not expect our estimates of C'' to agree with those for a Rayleigh-Taylor instability.

The variation of C' with the stability parameter Ra_3 (Figure 2.16) is similar to the variation of q' with Ra_1 that we observe for Newtonian viscosity (Figure 2.9). For non-Newtonian viscosity, three temperature dependences of viscosity are given for

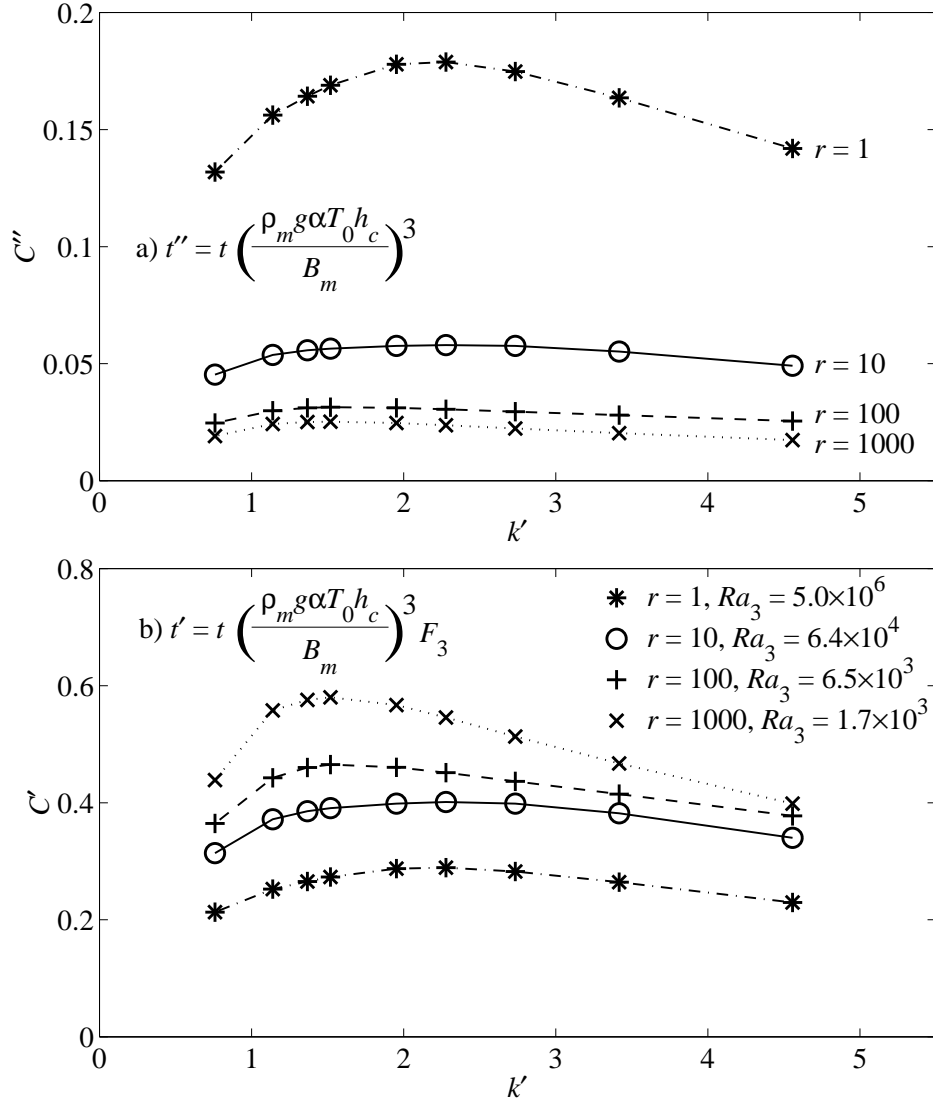


Figure 2.14: Plots of the dimensionless super-exponential growth rate, C'' or C' , versus dimensionless wavenumber, $k' = 2\pi/\lambda'$, with time scaled using (2.11) in (a) and (2.29) in (b). Thus, (b) scales rates with “available buoyancy.” We used an initially error-function temperature profile perturbed using (2.40) with $p = 0.2$.

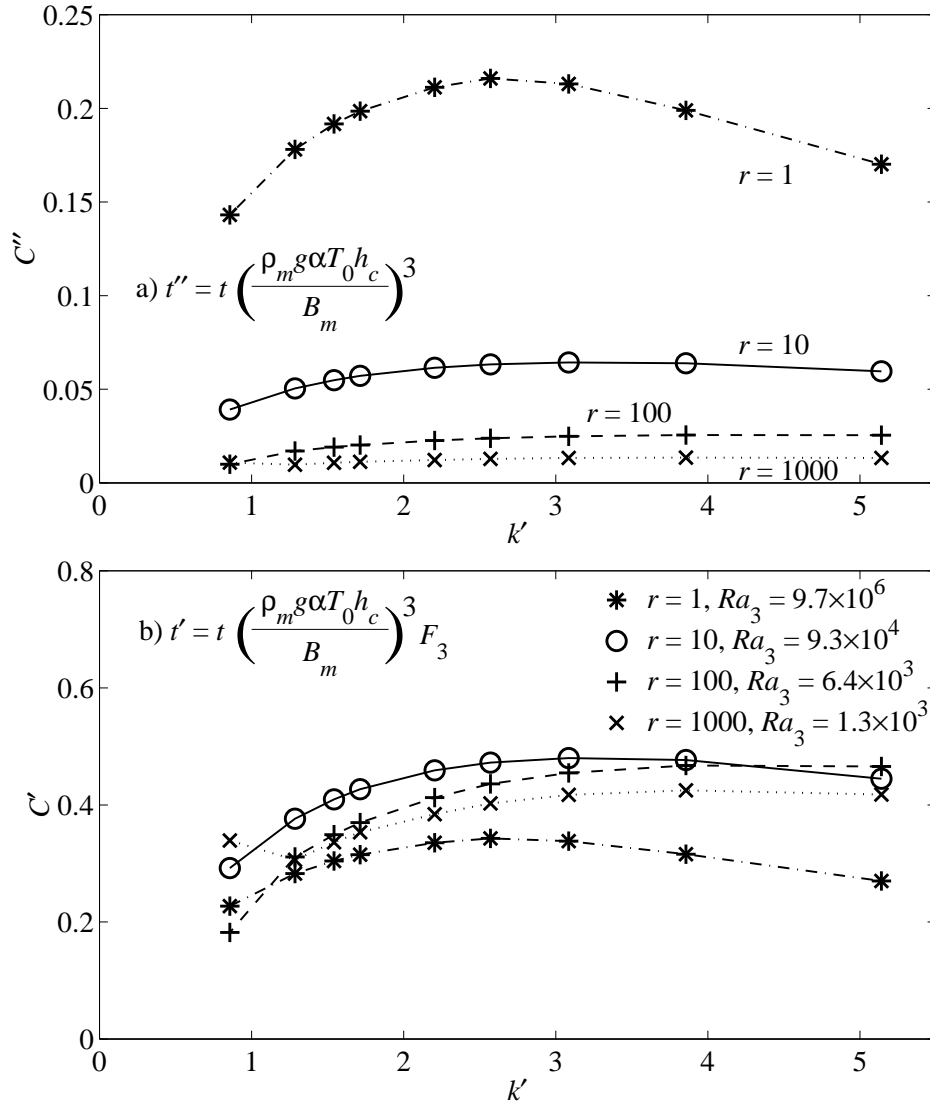


Figure 2.15: Similar to Figure 2.14, but for an initially linear temperature profile, perturbed using (2.40) with $p = 0.2$. Again, (b) scales time with the “available buoyancy,” while (a) does not.

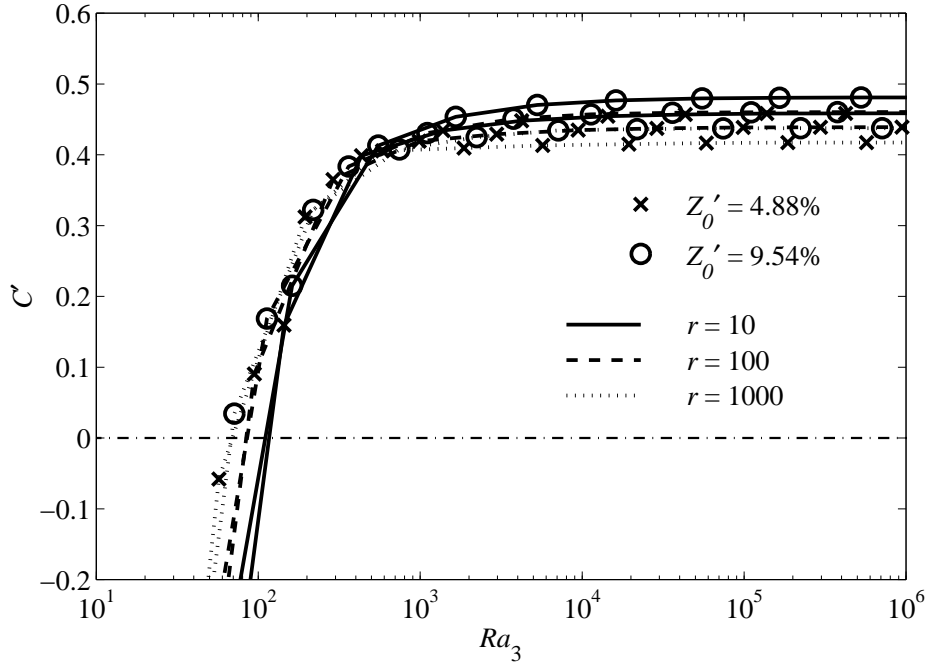


Figure 2.16: Plot showing how the super-exponential growth parameter, C' , scaled with the “available buoyancy” using (2.29), varies with the stability parameter, Ra_3 , for a layer with non-Newtonian viscosity ($n = 3$) and for $r = 10, 100$, and 1000 . We show calculations for two choices of the initial amplitude, Z'_0 , of the perturbation to an initially linear temperature profile; using (2.40) and $p = 0.10$ or $p = 0.20$, we generate perturbations of $Z'_0 = 4.88\%$ or $Z'_0 = 9.54\%$. We varied Ra_3 by varying B_m .

two different amplitudes of initial perturbations, Z_0 , and the value of Ra_3 , calculated according to (2.36), takes into account the magnitude of the perturbations. For all and for $Ra_3 > 1000$, we observe fairly constant values of C' equal to about 0.45. For values of Ra_3 less than about 100, the layer is convectively stable. The convective stability of a layer depends on the wavelengths at which it is perturbed. As we found for Newtonian viscosity, short wavelength perturbations are stable at smaller values of Ra_3 than are long wavelength perturbations (Figure 2.17), because they can be diminished by diffusion of heat in the horizontal direction. Long wavelength perturbations again promote increased instability because thermal diffusion in the vertical direction increases the driving buoyancy of the layer as the instability grows (Figure 2.17).

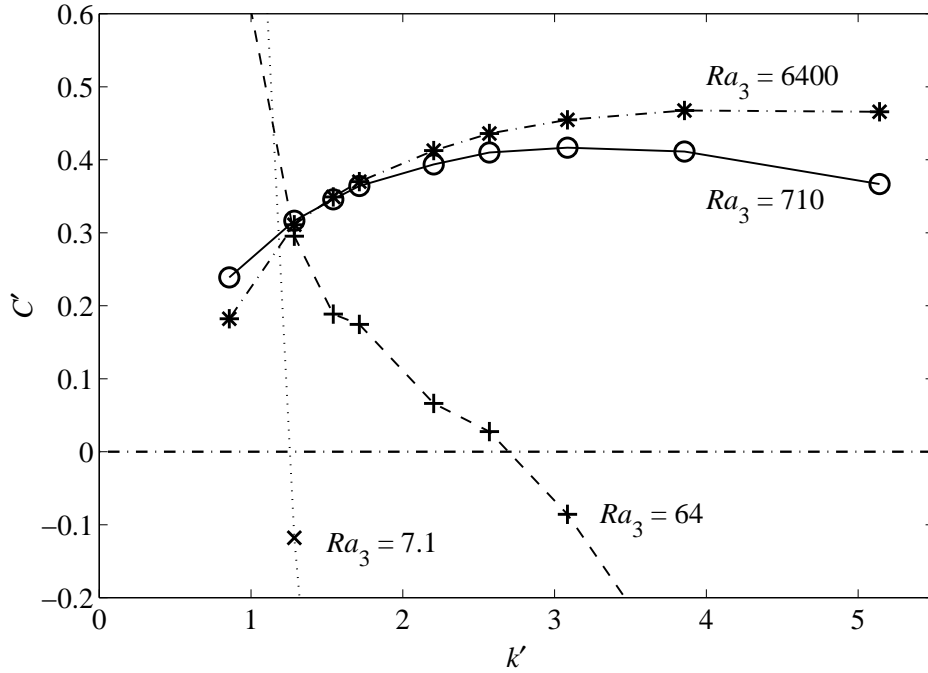


Figure 2.17: Plot of C' versus dimensionless wavenumber, $k' = 2\pi/\lambda'$ for an initially linear temperature profile, perturbed using (2.40) and $p = 0.2$. All curves use $r = 100$, and Ra_3 is varied by varying B_m . Time is scaled using (2.29) to include the “available buoyancy.”

2.6 Application to the Lithosphere

We have shown that the stability parameter, Ra_n , scales the vertical variations of density and viscosity with depth. We now estimate this parameter for the lithosphere to determine the conditions under which it might become unstable and how long a convective instability might take to remove the bottom portion of the lithosphere. To do this, we estimate the parameters relevant to the lithosphere. We use $\rho_m = 3300 \text{ kg m}^{-3}$, $g = 9.8 \text{ m s}^{-2}$, $\alpha = 3 \times 10^{-5} \text{ K}^{-1}$, and $\kappa = 10^{-6} \text{ m}^2 \text{ s}^{-1}$. If the mantle lithosphere varies in temperature between $T_s = 800 \text{ K}$ at the Moho and $T_m = 1600 \text{ K}$ at its base, the temperature variation across the potentially unstable mantle lithosphere is $T_0 = T_m - T_s = 800 \text{ K}$.

To estimate the “available buoyancy,” F_n , we assume a temperature profile for the lithosphere and apply laboratory measurements of the temperature dependence

of viscosity. The parameter B varies with temperature as:

$$B(T) = 3^{\frac{-(n+1)}{2n}} \left(\frac{A}{2}\right)^{\frac{-1}{n}} \exp\left(\frac{H}{nRT}\right) \quad (2.45)$$

where $R = 8.3 \text{ J K}^{-1}\text{mol}^{-1}$ is the universal gas constant, H is the activation enthalpy, and A is the experimental constant inferred from laboratory measurements that relate strain rates to a power of stress [Molnar, Houseman, and Conrad, 1998]. This relation can be made dimensionless using (2.20):

$$B'(T') = \exp\left(\frac{HT_0(1 - T')}{nRT_m(T_s + T_0T')}\right) \quad (2.46)$$

For both linear and error-function geotherms, we use (2.22), (2.45), and (2.46) to calculate B_m and F_n for values of H , A , and n given by Karato, Paterson, and FitzGerald [1986] and relevant to diffusion ($n = 1$) and dislocation ($n > 1$) creep mechanisms for “wet” and “dry” conditions (Table 2.1). The dislocation creep mechanism is applicable if stresses are greater than about 0.1 to 1 MPa, which is likely the case for convective instability. Hirth and Kohlstedt [1996] propose that the “wet” rheology is applicable below 60 to 70 km depth. For dislocation creep, the estimates of H in Table 2.1 differ from those of Hirth and Kohlstedt [1996] by less than 20%, but estimates of A for dry olivine are smaller by a factor of 5, and those for wet olivine can not be easily compared because Hirth and Kohlstedt [1996] give a stress exponent of 3.5. For diffusion creep, estimates of A depend significantly on grain size, which is not well known for the mantle. Because of uncertainties in A and n , we expect our calculations of B_m to also include significant uncertainty, making our ignorance of the presence of wet or dry conditions at the base of the lithosphere somewhat unimportant for this study. Our estimates of F_n , however, do not depend on A , and thus should be more reliable. The most uncertain parameters are then the thickness, h , of the mantle lithosphere, and the material strength at its base, B_m ; we leave these parameters to be determined in the following analysis.

To estimate stability and growth rates for diffusion creep, we first calculate Ra_1

Table 2.1. Estimates of B_m and F_n for various creep regimes and temperature profiles.

Creep Regime	n^\dagger	H^\dagger (kJ/mol)	A^\dagger ($\text{s}^{-1}\text{Pa}^{-n}$)	B_m ($\text{Pa s}^{1/n}$)	F_n (Error Function)	F_n (Linear)
Wet Diffusion	1	250	$1.5 \times 10^{-12\dagger}$	6.7×10^{19}	3.1×10^{-2}	8.5×10^{-3}
Dry Diffusion	1	290	$7.7 \times 10^{-10\dagger}$	2.6×10^{18}	2.6×10^{-2}	6.6×10^{-3}
Wet Dislocation	3	420	1.9×10^{-15}	1.9×10^9	1.3×10^{-4}	5.5×10^{-5}
Dry Dislocation	3.5	540	2.4×10^{-16}	1.9×10^9	2.3×10^{-5}	8.8×10^{-6}

[†]From *Karato, Paterson, and FitzGerald* [1986].

[‡]Assumes a 10 mm grain size.

using (2.37) as a function of η_m using the parameters values listed above and for values of h equal to 25, 50, 100, and 200 km. We do this for $F_1 = 3.1 \times 10^{-2}$ and $F_1 = 6.6 \times 10^{-3}$ to span the full range of “available buoyancy” given for diffusion creep in Table 2.1. Using the values of $q'(Ra_1)$ given in Figure 2.9 for $r = 100$, we use (2.25) to calculate the exponential growth rate, q , as a function of η_m . Exponential growth exhibits a doubling of the amplitude of an instability in a time given by $\ln(2)/q$, which we plot as a function of η_m in Figure 2.18. Because the growth rate scales inversely with viscosity, the doubling time scales with η_m , if η_m is small enough to yield a large value of Ra_1 (Figure 2.18). If η_m is sufficiently large that $Ra_1 \lesssim 50$ (Figure 2.9), however, exponential growth stops, and the doubling time becomes infinite. This critical viscosity varies with the lithosphere thickness, h (equation (2.37)). As a result, a thin unstable layer requires lower viscosity at its base to become convectively unstable than does a thicker layer (Figure 2.18).

Depending on the initial amplitude of a perturbation, several doubling times will be required for that perturbation to grow large enough to remove the bottom portion of the lithosphere. Thus, if convective instability requires five doubling times within, say, 10 million years, the (Newtonian) viscosity at the base of the lithosphere must be

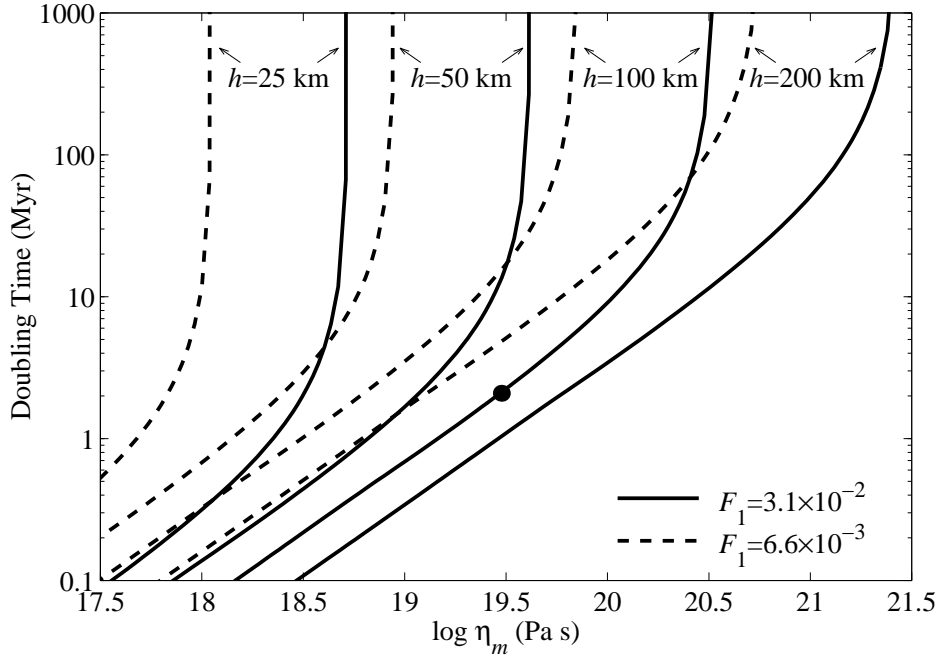


Figure 2.18: Plot of the time for an instability to double in amplitude, given by $\ln(2)/q$, as a function of the viscosity at the bottom of the layer, η_m , for exponential growth with Newtonian viscosity. The doubling time, given in millions of years, is calculated as described in the text for four layer thicknesses and the two most extreme values of F_1 given in Table 2.1 for diffusion creep, and other parameter values given in the text. The dot represents a solution showing that if $\eta_m = 3 \times 10^{19}$ Pa s and $h = 100$ km, an instability will double in size approximately every 2 million years. Such an instability will be removed in 10 million years if five doubling times are required for this to occur.

less than about 3×10^{19} Pa s for a 100 km thick mantle lithosphere and $F_1 = 3.1 \times 10^{-2}$ (dot on Figure 2.18). Thinner lithosphere or decreased “available buoyancy” requires smaller viscosities. Viscosity as low as $\eta_m = B_m/2 = 1.3 \times 10^{18}$ Pa s is suggested by laboratory studies (Table 2.1) for diffusion creep, which would allow mantle lithosphere thicker than about 50 km to rapidly become unstable. *Hager* [1991] used several geophysical observables to estimate that asthenospheric viscosities could be as low as 10^{19} Pa s but other authors suggest values closer to 10^{20} Pa s [e.g., *Mitrovica and Forte*, 1997]. This latter value permits only very thick (200 km) lithosphere to become unstable in 10 million years for the lower bound of “available buoyancy” (Figure 2.18, dashed lines) but still allows instability in 50 km thick lithosphere for

the upper bound of F_1 (Figure 2.18, solid lines). Thus, if viscosity is Newtonian, convective removal of the lithosphere’s base in a few million years is perhaps not unrealistic, but probably only where mantle lithosphere is more than 100 km thick.

To consider non-Newtonian viscosity applicable for dislocation creep, we calculated Ra_n as a function of B_m for dislocation creep under both wet ($n = 3$) and dry ($n = 3.5$) conditions. We again use the lithospheric parameters given above and new estimates of F_n (Table 2.1), and we consider perturbations with amplitudes only 10% of the thickness of the entire layer, $Z_0 = 0.1h$. We use the $r = 100$, $Z'_0 = 9.54\%$ curve in Figure 2.16 to obtain C' as a function of B_m , from which we calculate the dimensionless time to removal, t'_b using (2.32). We make this quantity dimensional using (2.29), and give its functional dependence on B_m in Figure 2.19 for both wet and dry olivine, four thicknesses, and the range of F_n given in Table 2.1. In applying the curve for $C'(Ra_3)$, which we calculated using $n = 3$, to dry conditions for which $n = 3.5$, we have assumed that the curve of $C'(Ra_n)$ is approximately the same for both $n = 3$ and $n = 3.5$. This assumption is perhaps not inappropriate because *Houseman and Molnar* [1997] find only a weak dependence of C'' on n for $n = 2, 3$, and 5.

Extrapolations of laboratory measurements to conditions at the base of the lithosphere yield B_m on the order of 10^9 Pa s^{1/n} for both $n = 3$ and $n = 3.5$ (Table 2.1). This value of B_m implies convective removal of the lower lithosphere in less than 1 million years for lithospheric thicknesses greater than about 25 km for wet conditions (Figure 2.19a), but 100 km for dry conditions (Figure 2.19b). These thicknesses, of course, depend on the actual value of B_m . Similarly, the “available buoyancy,” F_n , (Table 2.1) affects the “critical” thickness for convective instability. Decreasing F_n by a factor of two corresponds to increasing B_m by a factor of only $2^{1/n}$, as shown by (2.29), making variations in F_n less important for $n = 3$ or 3.5 than for $n = 1$. For $n > 1$, the time to removal also depends on the initial perturbation amplitude, Z_0 , to the $(1 - n)$ power, as in (2.32). As supposed by *Houseman and Molnar* [1997] and *Molnar, Houseman, and Conrad* [1998], perturbations with amplitudes half the lithospheric thickness may be possible for recently thickened lithosphere, which are five times the amplitude of those considered here. Multiplying Z_0 by a factor of 5

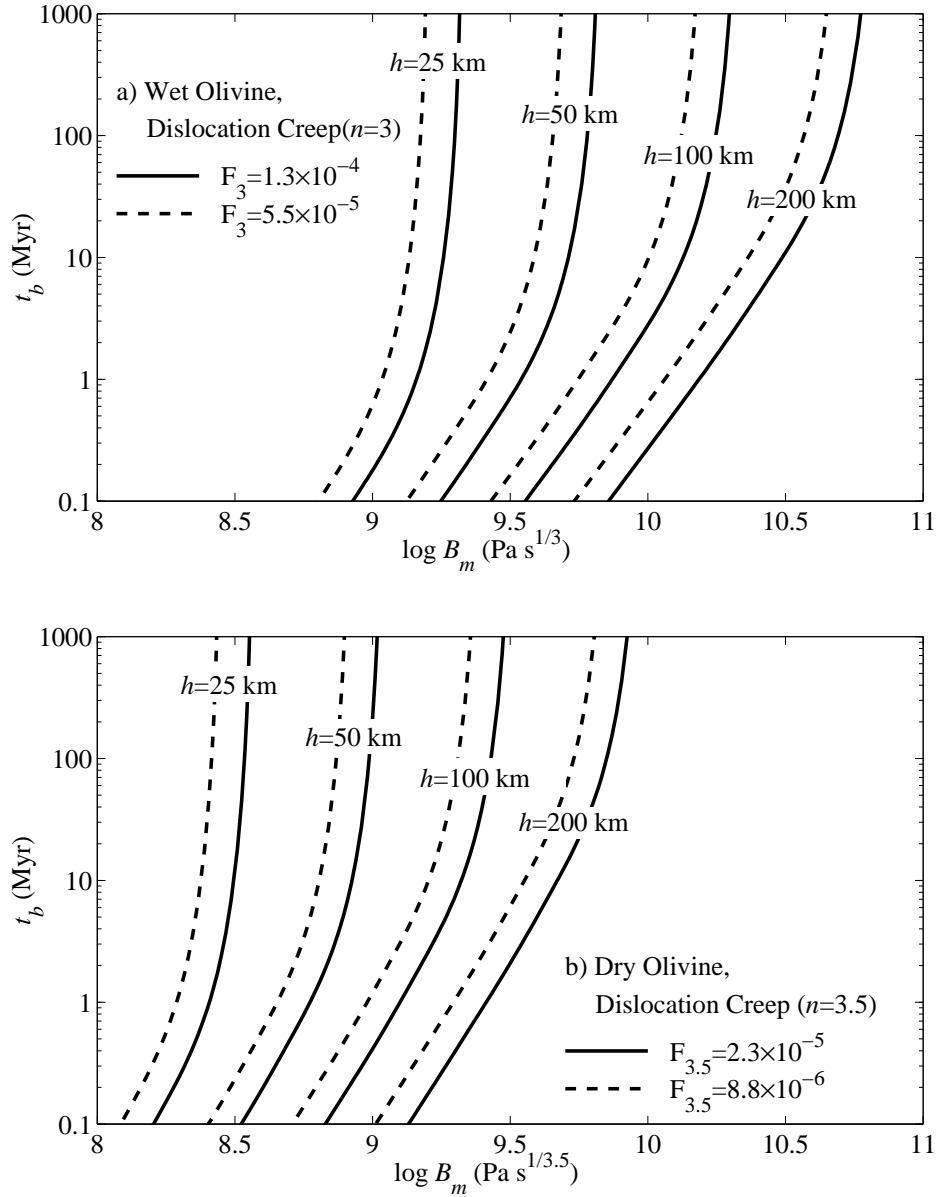


Figure 2.19: Plot of t_b , the time for an instability to become completely detached from an unstable layer, as a function of the rheological parameter at the bottom of the layer, B_m , for a non-Newtonian viscosity characterized by dislocation creep. The removal time, given in millions of years, is calculated as described in the text for both (a) wet conditions, for which $n = 3$, and (b) dry conditions, for which $n = 3.5$. Calculations are given for four layer thicknesses, the two values of F_n given in Table 2.1, and the other parameter values given in the text.

has the same effect as decreasing B_m by a factor of $5^{1-1/n}$, as shown by (2.32) if it is redimensionalized by (2.29). This shifts the curves in Figure 2.19 to the right by a factor of about 3, which expands the range of B_m that produces rapid instability for a given lithosphere thickness.

Some portions of the continental lithosphere have remained stable for long periods of the Earth's history. Many cratonic shields have undergone little or no deformation for more than a billion years [e.g., *Hoffman, 1990*]. Thus, continental lithosphere is generally stable; some additional mechanism is required for it to become unstable. One such mechanism could be mechanical thickening. If the mantle lithosphere is thickened along with the crust during an episode of horizontal shortening, the vertical length scales associated with a convective instability increase. Because the sublithospheric viscosity is not affected by such thickening, an increase in h has the effect of decreasing the time for an instability to occur (Figures 2.18 and 2.19). For certain values of h and η_m or B_m , increasing h by a factor of two can cause an otherwise stable lithosphere to become convectively unstable on short time scales. For example, if $B_m = 10^{10} \text{ Pa s}^{1/3}$ for dislocation creep of wet olivine, 50 km thick mantle lithosphere is convectively stable, but its lower part will be removed in 2 million years if it thickens by a factor of two (Figure 2.19a).

If viscosity is non-Newtonian, increasing the amplitude of a perturbation has the same affect as increasing the layer thickness, h , as discussed above. Thus, convective instability can be generated from a stable mantle lithosphere if large perturbations can be generated at its base. Horizontal shortening could help generate large amplitude perturbations through folding instability or localized thickening. Because horizontal shortening has already been associated with the initiation of convective instability through an increase in lithosphere thickness, as described above, or through a decrease in strength due to strain-rate weakening [*Molnar, Houseman, and Conrad, 1998*], it seems likely that horizontal shortening could initiate a convective instability at the bottom of the lithosphere.

Convective instability should continue to erode thickened mantle lithosphere until it is thin enough to be stable on long time scales. The bottom, weakest part will be

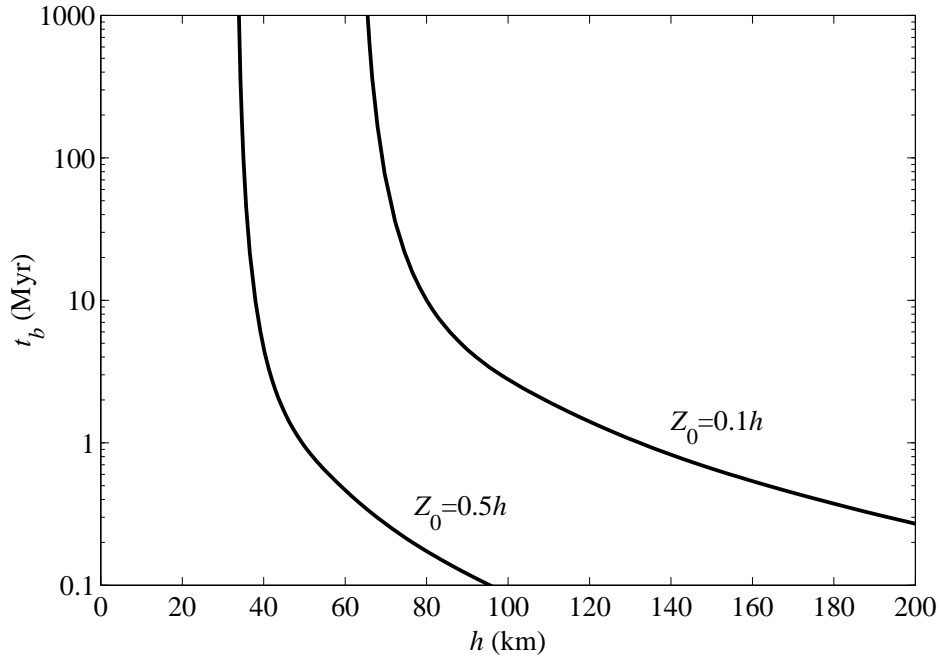


Figure 2.20: Plot of t_b , the time for an instability to become completely detached from an unstable layer, as a function of the thickness the layer, h . The removal time, given in millions of years, is calculated as described in the text assuming wet conditions ($n = 3$), $B_m = 10^{10} \text{ Pa s}^{1/3}$, $F_3 = 1.3 \times 10^{-4}$, and an initial perturbation amplitude, Z_0 , of either 10% or 50% of h . Other parameter values are given in the text.

removed quickly, but removal of the colder interior of the mantle lithosphere requires increasingly greater time [Molnar, Houseman, and Conrad, 1998]. To determine the thickness of a layer that will remain stable for a given amount of time, we plot the removal time, t_b , as a function of the layer thickness, h (Figure 2.20). We calculated t_b using (2.32) and the dependence of C' on Ra_3 (Figure 2.16), and assume wet conditions ($n = 3$), $B_m = 10^{10} \text{ Pa s}^{1/3}$, $F_3 = 1.3 \times 10^{-4}$, and the parameter values given above. If perturbation amplitudes are 10% of the mantle lithosphere thickness, a layer 65 km thick will be stable for a billion years. If this layer is mechanically thickened to 130 km, the first instability to grow should do so in about 1 million years (Figure 2.20), and should remove the basal part, about 16 km using the estimates of Molnar, Houseman, and Conrad, [1998]. With negligible diffusion of heat in this interval, perturbations at the base of the remaining 114 km thick layer should be

unstable and grow, but more slowly. This process should continue, with removal of basal layers at successively lower rates until a stable layer is achieved. If perturbation amplitudes remained only 10% of the layer thickness, the layer would eventually return to its original thickness, 65 km, but this will take a billion years (Figure 2.20). A thickness of 80 km, however, will be reached in only 10 million years. It is possible to make similar estimates for a variety of values of B_m by estimating the thickness of a layer that is stable on time scales of 10 million years from Figures 2.18 and 2.19 for a given value of B_m . This thickness is generally a factor of 1.2 to 1.5 times that of a layer that remains stable for a billion years (Figures 2.18 and 2.19). Thus, lithosphere that is at its stability limit and then thickened by a factor of two, should, in 10 million years, erode back to a thickness 20 to 50% larger than its original thickness. The lower end of this range applies to thinner layers (25 to 50 km) and the higher end to thicker layers (100 to 200 km).

This estimate is complicated by the dependence of both Ra_n and t_b the perturbation amplitude, which we expect to increase as a layer thickens. If, for instance, as h increased from 65 km to 130 km, perturbations grew from 10% to 50% of h , the thickness of the layer after 10 million years of convective removal will be about 40 km (Figure 2.20), only 60% of the original 65 km thickness. Thus, it is possible that mechanical thickening could lead to a net thinning of the mantle lithosphere because convective instability can remove more lithosphere than is accumulated by a thickening event. For this to occur, viscosity must be non-Newtonian and the mechanical thickening must generate a significant increase in perturbation amplitude.

We might also expect the temperature profile of a thickened layer to change as its bottom part is convectively removed. The base of the lithosphere should be removed soon after, or during, a thickening event, and should carry with it a significant fraction of the layer's "available buoyancy," leaving that layer overly cold, and therefore strong. Thus, we expect a decrease in F_n with each successive removal, slowing further unstable growth. This decrease in F_n is opposed by the diffusion of heat. Thermal diffusion associated with the juxtaposition of cold lithosphere and hot asthenosphere after a convective removal event should help replenish the "available buoyancy" by

increasing the amount of warm material. If thermal diffusion and the increase in perturbation size caused by thickening approximately balance the decrease in “available buoyancy” as successive instabilities occur, then the above estimates of the degree of convective thinning following mechanical thickening should apply. If a decrease in “available buoyancy” overwhelms the perturbation size increase, it will be difficult for the instability to grow sufficiently to remove a significant fraction of the lithosphere. On the other hand, if the increase in perturbation size is more important than the decrease in “available buoyancy,” thickened lithosphere could erode mantle lithosphere and eventually make it thinner than its original thickness.

2.7 Conclusions

The “available buoyancy” provides a simple scaling that approximates the rate at which a density instability may grow from a cold, dense fluid layer. Although the growth rates for several thermal structures have already been determined [e.g., *Conrad and Molnar, 1997; Houseman and Molnar, 1997; Molnar, Houseman, and Conrad, 1998*], they are necessarily complicated by the details of the temperature dependence of viscosity, non-Newtonian viscosity, and the functional dependence of temperature on depth within the layer. The advantage of the “available buoyancy” scaling is that it enables all of these “complications” to be included in a single scaling, so that an approximate determination of the growth rate can easily be calculated for a given temperature and viscosity structure. By comparing this growth rate to the slowing effects of thermal diffusion, we can assess whether a given thermal structure is convectively unstable.

Thus far, we have examined only unstable density structures that are generated by the thermal contraction of fluids at cold temperatures. For the deep mantle lithosphere beneath continents, an unstable density structure created by temperature may be stabilized by the addition of basalt-depleted, low-density peridotites [*Jordan, 1978; Jordan, 1981; Jordan, 1988*]. This structure, proposed to account for the observed stability of deep continental roots over billions of years, has been termed by *Jordan*

[1978] the “continental tectosphere.” Although our definition of the “available buoyancy” does not take chemical density differences into account, this should be relatively easy to do. Qualitatively, the addition of low-density material to a thermal structure should decrease the total “available buoyancy,” and thus slow growth. Care must be used, however, when determining the convective stability of density structures that are partially generated by chemical differences because only temperature-induced density variations are subject to smoothing by thermal diffusion. In the tectosphere, however, the compositional variations in density are not themselves unstable, so the stability analysis derived here should apply, if the appropriate “available buoyancy” can be estimated.

Because continental lithosphere is thought to be stable, at least on time scales of billions of years, some disrupting event must occur for it to begin to become unstable. We have shown that the lithosphere can move from a condition of convective stability to one of instability through the mechanical thickening of its mantle component. Because the degree of instability is proportional to the cube of the mantle lithosphere’s thickness, significant thickening can lead to instability, both by increasing the amount of negatively buoyant material in a given vertical column, and by decreasing the effects of thermal diffusion. In addition, if lithospheric material behaves as a non-Newtonian fluid, large-amplitude perturbations generated in conjunction with a thickening process, and weakening due to horizontal straining, can generate even more rapid convective removal after a thickening event. We estimate that 10 million years after mechanical thickening, it is possible that convective erosion could result in a mantle lithosphere that is only 60% as thick as it was before the thickening event. A smaller fraction of lithosphere is removed if the amplitude of perturbations does not increase significantly as the layer thickens.

Such convective removal should result in surface uplift of a few kilometers [e.g., *Bird, 1979; England and Houseman, 1989; Molnar, England, and Martinod, 1993*], followed by eventual extension, as is observed in several mountain ranges [*Houseman and Molnar, 1997*]. The replacement of cold mantle lithosphere by hot asthenosphere should also cause melting of portions of the remaining mantle lithosphere, causing

volcanism and possibly regional metamorphism. Trace element isotopic analysis of volcanism in previously thickened areas suggests that this volcanism is produced by the melting of continental lithosphere, not asthenosphere [e.g., *Fitton, James, and Leeman, 1991; Turner et al., 1996*]. This evidence is not consistent with some models that produce rapid surface uplift such as complete delamination of mantle lithosphere or mechanical thickening that does not yield instability. It is, however, consistent with significant, but not complete, removal of the mantle lithosphere by convective erosion, a processes that we have shown to be associated with previous mechanical thickening of the mantle lithosphere.

Acknowledgments. This work was supported in part by National Science Foundation grants EAR-9406026 and EAR-9725648, and by a National Science Foundation Graduate Research Fellowship. We thank U. Christensen, B. Hager, G. Houseman, R. Fletcher, and an anonymous reviewer for suggestions at various stages of this work that focused our thinking and clarified our arguments.